Precipitation behavior in an Al-Cu-Mg-Si alloy during ageing

M. Gazizov[1,2], C.D. Marioara[3], J. Friis[3], S. Wenner[3], R. Holmestad[1], R. Kaibyshev[2]

[1] *Department of Physics, Norwegian University of Science and Technology (NTNU), Trondheim, Norway*
[2] *Laboratory of Mechanical Properties of Nanostructured Materials and Superalloys, Belgorod State University, Belgorod, Russia*
[3] *Materials and Nanotechnology, SINTEF Industry, Trondheim, Norway*

Abstract

The precipitation behavior and aging response of an Al-4.9Cu-0.74Mg-0.51Si-0.48Mn-0.1Cr-0.08Ti-0.02Fe (wt. %) alloy was examined in detail after aging at 170°C with different dwell times up to 96 h. Deformation by 3%-stretching prior to aging was used to investigate the effect of dislocations on phase and hardness evolution and compared with the undeformed material. The small pre-deformation led to a slight decrease of peak strength due to reduced homogenous nucleation and lower overall precipitate number density. Strong interaction between different phases caused the formation of hybrid structures both in the undeformed bulk areas and on dislocations. These phases consist of different fragments of the GP zones, θ”- and θ’-phases from the Al-Cu system, GPB zones and S1-phase from the Al-Cu-Mg system, and β”-, β’-Cu, C- and Q’-phases from the Al-Mg-Si-Cu system. A new phase named C1, isostructural to the C-phase but having a different orientation with the Al matrix – $(010)_C//(010)_{Al}$, $[001]_C//[101]_{Al}$, has been found predominantly on dislocation lines, and to a lesser extent in hybrid precipitates in the bulk. Calculations of structural stability by density functional theory (DFT) were performed on experimentally found structures, consisting of a C-phase core in two different orientations, and having Cu segregations in GP-like structures at their interfaces with the matrix.

Keywords

Aluminium alloys; characterization; electron microscopy; phase transformations; hardness; modeling/simulations

1. Introduction

Age-hardenable Al-Cu-Mg-Si alloys are used as structural materials in aerospace industry due to the their unique combination of properties of high specific strength, high fracture toughness and excellent fatigue properties, satisfactory corrosion resistance, etc. [1,2]. These alloys are strengthened during ageing at elevated temperatures due to the

formation of nano-sized particles of different phases [1–4]. Magnesium and silicon additions significantly change the precipitation behavior and kinetics in Al-Cu alloys, and hybrid structures consisting of diverse phases belonging to the Al-Cu, Al-Cu-Mg and Al-Mg-Si(-Cu) systems can be formed [2,5,6]. Research using different examination techniques has been attempted in order to properly characterize the phase composition of these precipitates, their distribution, morphology and crystal structures [2,5–8]. However, some confusion and uncertainties have been found in the interpretation of the phase composition of the alloys due to similarities in precipitate morphology and possible formation of hybrid precipitates consisting of small fragments of different phases. For this reason, the co-precipitation mechanisms for the fragments of the different phases are still not well understood.

In Al-Cu-Mg-Si alloys, depending on Cu concentration and Mg/Si ratio, different phases belonging to one alloying system or even a combination of several systems form during artificial aging. It has been shown [2] that a Cu content in the range of 2.5-4.5 wt.% and a Mg/Si ratio (in wt. %) lower than ~1.73 will produce the equilibrium θ-, Q-phases, as well as pure Si particles at long aging times. In several Al-Cu-Mg-Si alloys [2,6], the prior precipitation sequence related with the θ-phase includes GP (Guinier-Preston) zones (or GPI), θ’’(or GPII) and θ’-phases [3,4,9–16]. Among these precipitates the disperse θ’-phase plates are highly efficient in strengthening [3,16,17]. The situation with the quaternary Q-phase having composition proposed in a range from $Al_3Cu_2Mg_9Si_7$ to $Al_5Cu_2Mg_8Si_6$ [18,19] is more complicated due to diverse metastable AlCuMgSi (or AlMgSiCu) phases identified in a wide compositional range of commercial Al-Cu-Mg-Si (2XXX series) and Al-Mg-Si-Cu (6XXX series) alloys [2]. A precipitation sequence, including the formation of QP and QC phases, was suggested in an alloy with composition close to Al-4Cu-1Mg-0.7Si-0.5Ag (wt. %) [7,20]. Liu *et al.* also reported [6] that the formation of the Q’’-type precipitates, crystal structure of which was not identified, contributed to the considerable increase in the ageing kinetics and higher strength at the early ageing stage of an Al-5.0Cu-0.3Mg-0.3Si (wt. %) alloy. It has been shown that heterogeneous nucleation of the θ’-phase on rod-like Q’’-type precipitates causes refinement of the former phase plates compared with a Si-free alloy in the peak-aging state [6].

Chemical compositions, crystal structures and morphology of the precursors of the Q-phase have been studied in details in Al-Mg-Si alloys with small Cu additions. GP-zones

(also called as pre-β'') are formed in these alloys at early aging stages [21]. The β'', β'-Cu, β'', L, C, S_{Si} and Q'-phases (AlMgSiCu-type phases) have been found in Al-Mg-Si-Cu alloys in a peak-aging state. Details of chemical composition, crystal structure, morphology and OR of these phases have been widely discussed in literature [19,21,30,22–29]. It was shown that the fragments of the different AlMgSiCu phases can co-precipitate forming hybrid structures and furthermore that Cu atoms tend to occupy certain sites at interfaces between these precipitates and the *fcc*-Al matrix [6,22,31–33]. In Al-Cu-Mg-Si alloys with high Cu/Mg ratios and relatively low Si contents, the formation of the S-phase, its precursors as well as σ-phases, take place [2,34,35]. A number of precursors of the S-phase have been mentioned in the literature, such as Guinier-Preston-Bagaryatsky (GPB) zones, S'' and S' [35–39], or S1 and S2 [40,41]. An overview of the nominal chemical compositions, morphology, crystal structures and orientation relationships (ORs) of these phases is summarized in Table 1. $\{200\}_{Al}$ projections of crystal structures of the phases belonging to different alloying systems are presented in Fig. 1.

The results of previous work detailed above point to a very complex precipitate configuration in the Al-Cu, Al-Cu-Mg and Al-Mg-Si-Cu alloy systems. Therefore, the goal of this work is to investigate the precipitate crystal structures formed in an Al-Cu-Mg-Si alloy, which has a composition at the border between the three mentioned systems during aging at 170°C, including the study of co-precipitation mechanisms in a relation with mechanical properties. The effect of pre-deformation by 3%-stretching prior to aging was also investigated, and precipitate evolution was compared with the undeformed state.

To identify the atomic column arrangements in the different phases all the images were taken in an $\{200\}_{Al}$ projection using high-angle annular dark-field scanning TEM (ADF-STEM). The atomic models were suggested based on atomic column Z-contrast, known crystal structures of various precipitates in the 2XXX and 6XXX Al alloy systems and phase construction rules for precipitates in the Al-Cu-Mg and Al-Mg-Si(-Cu) systems given in [25]. According to these rules, every Al atom has 12 near neighbors, every Mg atom has 15 and every Si has 9. It means that in the model every Al atom is surrounded by 4 atoms of "opposite" height (±0.203 nm), every Mg by 5 and every Si by 3 (making it a triangular site). Examples of such atomic columns arrangement in the S1-phase cross-section are shown in Fig. 1, where dashed lines (symmetry) indicate the near neighbors around Al,

Cu and Mg atoms. Interestingly, Cu was observed to be a triangular site (as Si) if located inside precipitates or GPB zones, or to have an Al local configuration when located at the precipitate's interfaces with the Al matrix, or if part of GPI zones and θ''-phase (Fig. 1). Also, it should be noted that Cu can take two different local atomic arrangements forming sub-units in the Al-Mg-Si-Cu alloys: in-between the Si atomic columns as in Q'- and C-phases, and replacing 1/3 of the Si atomic columns in the β'-Cu phase [42].

Density functional theory (DFT) has been applied to calculate the formation enthalpy of hybrid precipitate structures consisting of GP-like structures/Cu segregations and L precipitates involving fragments of the C-phase, in order to verify and understand the structural observations.

2. Experimental procedure

An aluminum alloy with the chemical composition of Al-4.9Cu-0.74Mg-0.51Si-0.48Mn-0.1Cr-0.08Ti-0.02Fe (wt. %, Mg/Si~1.45) was cast as cylindrical billets (Ø38×140 mm). The alloy was homogenized at 500°C for 24 h and hot rolled (~400°C) to 14 mm plates. Rectangular samples with sizes of 14×14×3 mm and flat "dog-bone" specimens with gauge sizes of 35×7×3 mm were cut from the central part of the hot-rolled billets using wire electric discharge machine. These specimens were solution heat treated at 500°C for 1 h, followed by water-quenching to room temperature. The flat "dog-bone" specimens were stretched immediately with an initial strain rate of 2×10^{-3} s^{-1} up to a fixed plastic strain of 3%, and machined to get rectangular samples with sizes of ~10×7×3 mm. The undeformed and 3%-stretched samples will hereafter be referred to as "undef" and "3%-def", respectively. The samples were then aged at 170°C for different ageing times in a range from 0.25 to 96 hours using a furnace with forced air circulation. Each sample was held at the aging temperature for 3 min to reach a thermal equilibrium, then aged for a certain time, and finally cooled in air.

Hardness measurements were performed on the broad flat surface of the rectangular samples using a Wilson Wolpert 402 MVD hardness tester at a constant load of 5 N and a loading time of 15 s. At least ten indentations were carried out in arbitrarily selected areas to determine the standard deviation of the hardness for each condition. The yield stress (YS), the ultimate tensile strength (UTS) and the elongation-to-fracture (δ) were measured using

an Instron 5882 tensile testing machine at an initial strain rate of ~10^{-3} s^{-1}. The YS, UTS and δ values were averaged using three samples from each condition.

Orientation imaging microscopy (OIM) with an automated indexing for electron back scattering diffraction (EBSD) patterns was carried out using a ZEISS Ultra 55 scanning electron microscope (SEM) equipped by a Nordif EBSD detector and a TSL OIM software. The surface for OIM analysis was prepared by mechanical polishing using a VibroMet 2 vibratory polisher. The average size of crystallites (grains) delimited by high-angle boundaries (HABs) (angle >15°) was measured by the mean linear intercept method, in which the longitudinal direction was parallel to the hot rolling direction for the "undef" state and stretching direction for the "3%-def" state. A Quanta 600FEG SEM was used for back-scattered electron (BSE) images of the constituent phases. The volume fraction of these constituents was determined by standard grid techniques.

TEM specimens were prepared by mechanical polishing to 100-200 μm thickness and electropolished with a solution of 2/3 methanol and 1/3 nitric acid at -30°C using a Struers TenuPol-5 twin-jet unit. TEM characterization was performed on a JEOL JEM-2100F microscope operated at 200 kV and equipped with an Oxford X-Max 80 SDD EDX detector. All the TEM and STEM observations were carried with electron beam parallel to an $<100>_{Al}$ zone axis. In this case, 1/3 of the $<100>_{Al}$ rods and 2/3 of the $\{200\}_{Al}$ laths/plates go through most of the TEM specimen with little overlap with the Al matrix, and can be imaged as "dots" and "rectangles", respectively. The volume fraction of the relatively coarse secondary phases approximated as particles having round shape was estimated as: $f = \frac{4}{3\sqrt{\pi}} S^{3/2} \frac{N_T}{(A_S + d_{eq}) \times t}$, where S is the cross-section area of precipitates, N_T is the number of counted precipitates, A_S is the TEM image area, $d_{eq} = 2\sqrt{\frac{S}{\pi}}$ is the equivalent circular diameter of precipitates in each TEM image, t is the foil thickness. The mean f and d_{eq} magnitudes and their standard deviations were calculated using the average S value linked with the precipitate size distribution in each TEM image. The density of lattice dislocations was estimated using intercept relationship as $\rho_d = \left(\frac{n_1}{L_1} + \frac{n_2}{L_2}\right)\frac{1}{t}$, where n_1 and n_2 are the numbers of intercepts on the sets of orthogonal lines of total lengths L_1 and L_2 in TEM images. The foil thickness was determined by the convergent beam electron diffraction

(CBED) method based on Kossel-Möllenstedt fringe oscillations [15,16,43,44] and averaged using at least three measurements for each TEM image.

A JEOL ARM-200F microscope equipped with a probe-aberration corrector and JEOL ADF-detector was used to examine the crystal structure of the precipitates formed in the aged samples. A spot size of 0.08 nm, 27 mrad convergence semi-angle and collection semi-angles of 35-149 mrad were used to acquire high-resolution ADF-STEM images along the $<100>_{Al}$ zone axis. These images contain projected locations of atomic columns of matrix and precipitates viewed in cross-section, providing information about the rod/lath/plate-shaped precipitate crystal structures. Identification of atomic columns chemistry is possible because ADF-STEM images contain atomic number (Z) contrast [45]. Fast Fourier transform (FFT) filtering has been applied to all images to reduce noise with periodicity shorter than ~0.14 nm.

The availability of solute for precipitation was calculated with the Thermo-Calc™ software with the TCAL1 database. The DFT calculations of the formation enthalpies for hybrid structures were performed with the Vienna Ab initio Simulation Package (VASP) [46] using the Perdew-Burke-Ernzerhof (PBE) exchange-correlation functional [47]. A gamma-centered k-point mesh was used in all calculations with a maximal k-point distance of 0.18 $Å^{-1}$ and a plane wave energy cut-off above 400 eV. The Methfessel-Paxton method of 1_{st} order was applied for atomic position relaxations with maximum force of 0.001 eV/Å [48] and a smearing factor of 0.2. For accurate energies, all relaxations were followed by a static calculation using the tetrahedron method with Bloch corrections.

3. Results

3.1 Mechanical properties

Hardness evolution as a function of logarithmic time and tensile curves in some specific stages of the "undef" and "3%-def" samples are presented in Figs. 2a and 2b, respectively. It is seen that the 3%-stretching of the as-quenched condition does not have a noticeable effect on hardness, as both the pre-deformed and undeformed material have a hardness level of ~83 HV. A tendency to form three hardness peaks during artificial aging is observed in the both alloy states. Aging at 170°C leads to an initial fast hardening response and the formation of a short hardness plateau up to 1 h, with similar hardness values of 120-130 $HV_{0.5}$ in both "undef" and "3%-def" samples, associated with the first peak (Fig. 2a).

The next increase in hardness seems to start at the same aging time, but the maximum is reached later in the "undef" state compared to the "3%-def" state, which is wider in shape and lower in absolute magnitude. This effect is marked as a second peak. The third peak is higher in the "undef" state, whereas it is less pronounced in the "3%-def" state. A loss of hardness during over-aging occurs with a similar rate in both "undef" and "3%-def" states, with the latter maintaining lower hardness values. All these effects can be associated with the stages of the precipitation evolution during aging [1,3,4].

Some specific ageing conditions chosen for tensile properties measurement (Fig. 2b) shows that the tensile curve shapes as well as the strength characteristics depend on the aging conditions. The alloy in the as-quenched and under-aging conditions exhibits a distinct strain hardening up to a high strain. Repeating oscillations that are associated with the Portevin-Le Chatelier (PLC) effect attributed to the dynamic strain aging in aluminum alloys [44] appear during the strain hardening stage in as-quenched and under-aging "3%-def" samples. Considering tensile properties in general, YS of the "3%-def" in the 1 h under-aging state is lower than in the "undef" state. The similarity in hardness and UTS values shows the reliability of both methods to determine aging stages. It is seen that the hardness values in different aging stages cannot be directly related with the YS values, but instead relate to the relative changes in UTS values. Maximum YS and UTS values and elongation-to-fracture for the alloy in peak-aging stages reach to ~405 MPa, ~450 MPa and ~9.8% for "undef" and ~390 MPa, ~430 MPa and ~8.7% for "3%-def" conditions, respectively. These results are commensurable with properties for other Al-Cu-Mg-Si alloys having similar chemical compositions [1,6]. Aging times of 0.25, 1, 16 and 96 h, corresponding to under-aged, peak-aged and over-aged conditions were chosen for subsequent TEM characterization.

3.2 Microstructural analysis

The initial microstructure of the alloy after solution heat treatment (not shown) and consists of grains having average size of ~113 and ~56 μm in the longitudinal and transverse directions, respectively, and fraction of HABs of ~80%. Different levels of a precipitate hierarchy can be identified: (1) coarse primary particles (agglomerates of bright particles in the BSE-SEM image, Fig. 3a)); (2) dispersoids (Figs. 3b and c); and (3) nano-sized precipitates appearing during aging (shown further). The coarse primary particles usually

have irregular cross-sections. Their volume fraction and equivalent circular diameter were estimated to be 2.0±0.4% and ~2.3 μm, respectively. Dispersoids are non-uniformly distributed in the matrix. Their estimated equivalent circular diameter was 90±25 nm. The volume fraction is dependent on the presence of coarse primary particles, and varies from 0 to ~2.7% in regions close to and far away from primary particles, respectively. The EDS map in Fig. 3c reveals that Mn, Si, Fe and Cr are present in dispersoids. It is seen that some inclusions, which are, in addition to these elements, also enriched by Cu, were attached to the dispersoids. Because of there is no other alloying elements correlating with the Cu distribution, we suggest that these precipitates are the θ-phase (Al_2Cu, I4/mcm, $a = b = 0.607$ nm, c = 0.488 nm [49]).

Simulations of equilibrium phase composition at 500°C using the Thermo-Calc software predicts the presence of the τ_1-phase (with , F-43m, $a = 1.092$ nm [50]), $Al_{12}(Mn,Fe)_3Si$ (Im-3, $a = 1.23$ nm [49]) and θ-phase with volume fractions of 0.26, 1.11 and 1.62 %, respectively. The chemical composition of the matrix was predicted to be Al-3.71Cu-0.74Mg-0.28Si-0.03Mn-0.08Ti with Mg/Si~2.64 (in wt. %, or Al-1.61Cu-0.83Mg-0.27Si-0.02Mn-0.05Ti in at. %). Cr and Fe contents in the matrix were calculated to be less than 0.001 wt. %. The decrease of Cu, Mn and Si contents in the matrix are consistent with the results of electron microscopy showing the presence of dispersoids enriched by these elements (Fig. 3c). The EDS map in Fig. 3c shows that Mn and Si are consumed from solid solution to form $Al_{12}(Mn,Fe)_3Si$ dispersoids, whereas the BSE-SEM images reveal the presence of bright coarse primary particles (Fig. 3a) tentatively identified as the θ-phase. No experimental evidences of the presence of the τ_1-phase have been found. Consumption of Si from the solid solution to form equilibrium dispersoids pushes the alloy matrix composition toward the Mg/Si ratio of ~2.64 corresponding to the (θ+β(Mg_2Si)) or even (θ+β+S+(σ)) phase fields [2].

3.3 Precipitate microstructure

TEM shows that dislocations naturally occur in the “undef” condition. They are non-uniformly distributed in the Al-matrix and predominantly observed in regions close to grain boundaries, coarse primary particles and dispersoids (Fig. 3c). The average ρ_d was measured to be ~2×10^{13} m^{-2} in these regions. Some dislocations were found in form of helices and loops. A similar tendency to form helical dislocations as well as loops was observed in an as-

quenched Al-Cu-Mg-Si alloys with decreased Si content [34]. Pre-deformation by 3%-stretching leads to a large increase in dislocation density and regions of their presence expanded, but dislocation-free fields can still be found in the "3%-def" condition. The ρ_d value was found to reach 10^{14} -10^{15} m^{-2} in the densest areas.

Obtained results show that the precipitation behavior was similar in dislocation-free regions and along dislocation lines in both "undef" and "3%-def" states (see Fig. 4). For this reason, the crystal structures of the precipitates discussed below do not differ between the "undef" and "3%-def" samples, and a distinction between these two states will not be made.

3.3.1. Under-aging state.

Representative (S)TEM images, showing a general evolution of precipitate morphology and crystal structure in under-aging states, are given in Figs. 4a-d, 5 and 6. Close examination reveals the presence of two precipitate groups categorized by morphology in the TEM images taken along $<100>_{Al}$ directions. The first group is associated with precipitates formed in dislocation-free regions. Tprecipitates appearing as diffuse dark spots in the bright field images with typical contrast originating from local elastic strains, as well as rod-shaped precipitates (Fig. 4a and c).

Solute clusters containing Cu (Fig. 5a) are clearly visible in ADF-STEM images, in addition to single Cu atomic columns along $<100>_{Al}$ direction, GP zones (which we define as a row of Cu columns creating an enriched $\{100\}_{Al}$ plane) and GPB-zone units (Fig. 5b). The Cu atoms also form ordered rod-like structures in the *fcc*-Al matrix shaped as a capsule (or tube) with diameter of 1-3 nm as shown in Fig. 5c. The formation mechanism of such Cu capsules is unknown, but it can be the result of heterogeneous nucleation and growth of monoatomic layers (GP-like structures) due to matrix distortions around Mg-Si enriched *fcc*-Al matrix. The tendency of Cu-enriched shell formation around other metastable precipitates is also demonstrated below in a current section.

The cross-sections of rod-shaped precipitates and suggested atomic models are shown in Figs. 5d-h. It is seen that all precipitates have hybrid and, sometimes, local disordered structures. The internal areas are occupied by the ordered fragments identified as well-known structures belonging to the Al-Mg-Si(-Cu) alloys (β" (eye), β'-Cu and C-phases [19,21–29]) and Al-Cu-Mg alloys (GBP zones [49,51]). Co-existence of small fragments of the C-phase in one precipitate is associated with the disordered L-phase. It is seen that GPB

zone units and GP-like structures have a tendency to form along the interfaces between the agglomerates of these fragments and Al matrix.

The second group of precipitates in under-aging state form continuous and somewhat jagged bands along dislocation lines (Figs. 4b and d). Similar decoration of dislocations by precipitates was observed in Al-Mg-Si alloys after 10% pre-deformation followed by aging at 190°C [52]. ADF-STEM images in Fig. 6 show precipitates formed on dislocation lines projected to $<100>_{Al}$ directions in the "3%-def" sample. The position of the dislocation lines can be identified by strip-type precipitates, as well as by a glow indicating segregation of the heavier elements such as Cu along the dislocation line. The formation of GP zones and θ''-phase plates having $\{200\}_{Al}$ habit planes is observed along dislocation lines (Figs. 6a and b). The heterogeneous nucleation of these phases along the dislocations differs from their nucleation in the bulk and commonly presented in the literature, where the tendency to homogeneous nucleation in matrix is observed due to the coherent nature of their interfacial boundaries and small difference from crystal structure of the Al matrix [3]. The formation of the Cu arrangement belonging to the C-phase was found in ADF-STEM images and corresponding FFT pattern (Fig. 6b), showing the similar distribution of diffraction streaks (marked by arrows) as observed in [24].

The projection of a dislocation loop decorated by precipitates in the "3%-def" sample after 1 h aging is presented in Fig. 6c. Precipitates nucleated on a segment of the dislocation loop are overlapped by the Al matrix, preventing their crystal structure to be clearly observed. Therefore, the remaining segment (without matrix overlap) was used to identify the decorating phases. It is revealed these precipitates are very diverse, being composed of fragments from a number of different metastable phases belonging to the Al-Cu, Al-Cu-Mg and Al-Mg-Si-Cu systems. Some disordered regions and local fragments contain only Cu arrangements in phases, as θ'' and S1 (in Al-Cu(-Mg) alloys), and others are based on both Cu arrangements and Si-networks as in β'-Cu, Q'- and C-phases (in Al-Mg-Si-Cu alloys). It is also seen that different phases decorate dislocation lines depending on the orientation of its segments in the $\{200\}_{Al}$ projection: S1-phase precipitate [40] down to one unit cell size in projection can be found along the dislocation segments with projection line parallel to the $\{210\}_{Al}$ planes. A crystal structure containing Cu arrangements and Si-networks in projection similar to the C-phase, but having unique orientation in Al matrix, was found in

both “undef” and “3%-def” states. An example of this crystal structure is presented in the suggested atomic model of Fig. 6c, named C1-phase. This orientation can be characterized as a 45° rotation around the *b* axis of the C-phase, when adopting the unit cell description from literature [27]. The unique disordered precipitate occupies a dislocation segment parallel to $\{220\}_{Al}$ planes. Cu segregation can be found along its interfaces. The OR between this unusual phase and *fcc*-Al matrix, is identified to be: $(010)_{C1}//(100)_{Al}$, $[001]_{C1}//[011]_{Al}$.

β’-Cu and Q’-phase has also been observed to locally decorate the dislocation segment, with typical orientations as reported in the literature [21–23,42].

3.3.2. Peak-aging state.

Figs. 4e and f show the typical morphology and distribution of precipitates in “undef” and “3%-def” samples after peak-aging, respectively. The precipitate microstructure can be characterized generally as follows. The rod-shaped particles become coarser than in the under-aged state, and particles, having plate-/lath-shape morphology with $\{200\}_{Al}$ habit planes which were not observed in the under-aging state, appear In the SAED patterns (insets in Fig. 4e and f), the strong diffraction streaks in $<100>_{Al}$ directions and “crosses” in the $½\{220\}_{Al}$ positions are associated with nucleation and growth of θ’-phase from the Al-Cu system [2,4,15,16]. This phase is dominant in the peak-aging state.

Circles in Figs. 4e and f show hybrid precipitates consisting of inter-grown plates and rods. This may indicate that rods provide nucleation sites for the plates, as only rods are observed to exist in the under-aged state, consistent with earlier observations [32].

It is seen in Fig. 4f that rod- and plate-like precipitates have a tendency to heterogeneously nucleate at or close to the interfaces between dispersoids and *fcc*-Al matrix because of solute segregations or presence of dislocations pinned by the dispersoid particles [1,4].

ADF-STEM images and corresponding FFT patterns for different precipitates and hybrid structures at peak-age are shown in Figs. 7 and 8. Some FFT patterns are noisy due to the prevailing disorder character of atomic column distribution in the precipitate crystal structures [52]. The θ’-phase plates, having $\{200\}_{Al}$ habit planes, and different hybrid structures containing this phase are represented in Figs. 7a-d. For θ’ plates with thickness about 1-1.5 nm the connection with the GPB zone units is often observed at the semi-coherent (narrow) interface of the plates. The bulk structure of these thin θ’ plates is defect-

free and matches with the well-established Silcock model [12–14,49,53]. Two columns, marked with red circles in Fig. 7a, are sites of triangular symmetry most commonly occupied by Si. Significant Si segregation at coherent θ'/Al interfaces have been observed earlier, and a strong thermodynamic driving force favoring Si partitioning to Cu sites in bulk θ' plates has been predicted by first principle calculations [12]. For this reason, the Si occupation identified in Fig. 7a is plausible.

Fig. 7b shows the presence of the θ' plates with stacking faults [53]. The formation of the θ'-C complexes early described in [32] have been also found (Figs. 7c and d). It is interesting to notice that both the Cu arrangement in the θ'-phase and the Si-network in the C-phase are observed as hexagonal with apparent ~0.4 nm plane periodicity in $\{100\}_{\theta'}$ and $(010)_C$ projections (Fig. 7c and d). It seems that C precipitate hinders the coarsening process of the θ'-phase associated with thickening ledge migration with height of half a unit cell along the broad plate surfaces [3,14].

Another example of a hybrid precipitate is presented in Fig. 8a. It is a C-phase platelet extending along $[001]_C$, with a one-unit cell width core and GP-like Cu segregations along both broad coherent interfaces. Similar GP-like structures were observed at coherent θ'/Al interfaces in Fig. 7. It has been revealed [14] that the interstitial positions in the θ' structure along the θ'/Al interfaces are filled due to high local Cu concentration in solid solution in early stages of plate growing in the Al-Cu alloys. Thus, the broad θ' plates interfaces are similar to the GP-like structure, which is associated with the thickening of θ' plates due to redistribution of these interstitial atoms on the ledge migration front. For this reason, one can speculate that similar GP-like structures at interfaces between AlMgSiCu precipitates and Al matrix could become preferable sites for heterogeneous nucleation of the θ'-phase. It is worthy to note that these type of hybrid precipitates consisting of C platelets and GP-like structures were also found in under-aging states (Fig. 5h)

Other examples of hybrid AlMgSiCu precipitates in the peak-aging state are presented in Figs. 8b and c. One precipitate contains two unit cells of β'-Cu phase showing the hexagonal network with columns occupied by 2/3 Si and 1/3 Cu in the projection plane (Fig. 8b). The β'-Cu part is surrounded by a disordered shell incorporating GPB zone units.

The hybrid precipitate in Fig. 8c consists of three identified structures corresponding to two fragments of the C-phase (or L) with a separate hexagonal Si-network, and one fragment

of β’’-phase with Cu atoms into the Si3/Al sites (Fig. 1) [22]. Cu atoms also tend to segregate between the different fragments of AlMgSiCu phases, where they form disordered structures (Fig. 8c), in addition to their segregations and formation of the θ’-phase fragments in the outskirt regions of hybrid precipitates.

String-type precipitates along dislocation lines are presented in Fig. 9. In addition to the precipitates, the exact position of dislocation lines in $\{200\}_{Al}$ plane projection can be identified by Cu segregations. The same types of metastable precipitates as in the early aging state are observed at the peak-aging states, but having coarser morphology. Similar tendency to occupation of dislocation line segments by different AlMgSiCu and AlCuMg precipitates depending on orientation in projection plane is revealed. In addition, coarse θ’-phase plates can be found. The C1 precipitate (Fig 9) is observed to form predominantly on dislocations in under- and peak-aging states. A few hybrid precipitates consisting of the C1-phase can also be found in bulk matrix, but the fraction is much lower compared with the appearance along dislocations. A common feature is that the C1-phase can be rarely found in the core of hybrid precipitates being surrounded by thick shell of other phase fragments. The unusual orientation of this precipitates has been roughly estimated using the Cu arrangements, which is similar to the C-phases, but turned on ~45°. In this case, the prismatic planes of hexagonal Si-network in the basal plane projection are parallel to the $\{410\}_{Al}$ and $\{220\}_{Al}$ planes, which coincides with the Si-network in Q-phase with OR3 observed in work [28].

3.3.3. Over-aging state

Figs. 4g and h represent ADF-STEM images of microstructure in the “undef” and “3%-def” samples after 96 h aging, respectively. It is seen that the rod- and plate-shaped particles grow thicker and longer during over-aging, that leads to decrease in their number density. The number density of rod-shaped precipitates in dislocation-free regions for the “3%-def” samples is lower in comparison with the same region in the “undef” sample. The tendency to heterogeneous nucleation of plate-shaped particles on dislocation lines and on AlMgSiCu precipitate interfaces is more pronounced.

ADF-STEM images of precipitates in dislocation-free regions in the over-aging state are presented in Fig. 10. Examination of these images shows that most precipitates consist of θ’-phase plates having faults and inter-growth of C-phase. It is seen in Fig. 10a that fraction and length of hybrid precipitates based on these phases also increase. The separate rod-

shaped precipitates usually have disordered structure consisting of the common hexagonal Si-network and fragments of Cu arrangements belonging to the C- and Q'-phases (Fig. 10b). In some cases, the Si-network is interrupted to form discrete local fragments (Fig. 10c). The most apparent change in phase fraction in dislocation-free regions is disappearance of the β"- and β'-Cu phases, as well as GP-like structures. However, Cu segregations having disordered structure still exist along interfacial boundaries of the AlMgSiCu. GPB zone units are commonly found at these interfaces despite being less stable in nature than S1- and S2-phases in Al-Cu-Mg alloys [36,40]. No formation of σ-phase [54] and pure Si particles was observed.

An example of the string-type precipitate along a dislocation line segment in the over-aging state, presented in Fig. 11, shows a complex phase composition. Fragments of different phases belonging to Al-Cu, Al-Mg-Si systems can be identified as θ', β'-Cu and S1-phases, as well as C1-phase with the unusual orientation. It is seen that this C1-phase connects to fragments of Q'-phase through a common Si-network with orientation corresponding to one of the six ORs for the equilibrium Q-phase found in the literature [28]. In general, the fraction and sizes of string-type precipitates increase in comparison with the peak-aging state. The GPB zone units and Cu segregations can be found in large numbers at interfacial boundaries.

4. Discussions

4.1 DFT investigations

Analysis of ADF-STEM images revealed that Cu tends to segregate along interfacial boundaries between different AlMgSiCu-type precipitates and *fcc*-Al matrix. The hybrid precipitates consisting of the C- and C1-phases with Cu segregations at the interfaces were frequently observed in present alloy. The formation of these hybrid precipitates seem to be energetically favorable due to accommodation of the misfit strain between precipitate and matrix. For example, it has been reported that Cu segregations form at the habit planes of lath-shaped precipitates in overaged states to accommodate the lattice misfit with the Al matrix in lean Al-Mg-Si alloys with trace Cu additions [33]. Here Cu atoms occupy certain sites at the interfaces between AlMgSiCu-type precipitates and *fcc*-Al matrix [6,22,32,42]. In our work, the formation enthalpies were calculated for two types of hybrid structures corresponding to two different orientations of the GP-like structures/Cu segregations: first,

normally oriented C-phase (with cross-section along <100>$_{Al}$) with Cu segregation at one or both habit planes as shown in Figs. 9 and 8a respectively. The second is the C1-phase with the unusual {110}$_{Al}$ habit plane and with Cu segregation as shown in Figs. 6c and 9. Modeled structures and calculated formation enthalpies with DFT are presented in Fig. 12. Since VASP is a periodical DFT code, the structures I-III and IV-V are considered as infinite {200}$_{Al}$ and {220}$_{Al}$ laths/plates, respectively. The difference between structures II/III and I, as well as between structure IV and V is the absence of the GP-like structures/Cu segregations along broad coherent interfaces between precipitate and *fcc*-Al matrix. Atomic arrangements for modeled structures II, III and V have been experimentally observed in the studied alloy at different aging states (see Figs. 6c, 8a and 9). The structures I and IV are constructed purely for comparison, to understand the influence of Cu interface segregation on the stability of the structures. It is seen in Fig. 12 that the formation enthalpy is lower for both orientations of the lath-shaped precipitates with the Cu segregations or layers along broad interfaces. It also demonstrates the tendency in decrease of enthalpy if the Cu atoms/layers occupy both sides of the laths. The formation of the {220}$_{Al}$ C1-phase laths without Cu segregations is the least favorable case. Thus, DFT calculations are in good agreement with the TEM results, as structures I and IV have higher formation enthalpy and are not found in the experimental observations. It should be noted that the GP-like structures or atomic columns with full occupation of Cu atoms were used in calculation. However, it was shown [9] that the GP zones comprising 40-50 at. % Cu are most stable in an Al-4 at. % Cu alloy. We suppose that different Cu atomic column occupancy in the GP-like structures can affect the accuracy in the enthalpy calculation, but it is clear the tendency is a decrease in formation enthalpy with increasing Cu segregation.

4.2 Relationship between precipitation behavior and strength

The influence of pre-deformation on YS values and the curve shape related to hardness evolution during aging (Fig. 2) are shown in Fig. 13a. In accordance with the experimental observations, three hardness peaks can be identified in both alloy states, despite of the fact that the second peak is less pronounced in the "3%-def" state. It should be noted that a similar splitting of the hardness peaks have been previously reported [6]. Three hardness peaks can be associated with the evolution of the phase composition during aging (Table 2) and superposition of the strengthening effect related to these precipitates. In

general, precipitate strengthening contributions depend on precipitate type, their morphology and distribution [1,4,44].

Despite that the experimental data collected in this work does not allow for an estimation of the exact precipitate strengthening contributions to the YS values, they can be schematically drawn using our current observations. Strengthening contributions from different mechanism are shown in Figs. 13b and c for "undef" and "3%-def" states, respectively. For simplicity, the total strength is presented as an additive sum of strengthening contributions from different precipitate types, solid solution and dislocation strengthening. Dispersoid strengthening is ignored due to relative low and constant contribution to the overall strength of the alloy during aging [1,3,4,44]. In Figs. 13b and c, an increase in the precipitate contribution is associated with nucleation and growth of certain precipitate types, while a decrease corresponds to their coarsening and/or dissolution [1,4,44]. Dislocation and solid solution strengthenings decrease with increased aging time due to recovery processes occurring at the aging temperature and depletion of alloying elements from the matrix, respectively. It is seen in Fig. 13b and c that the first, second and third peaks have been associated with the formation of clusters, rods/laths (AlMgSiCu phases) and plates (θ'-phase), respectively. In general, the aging curve shapes in "undef" and "3%-def" states can be explained by the influence of pre-deformation on kinetics and distribution of AlMgSiCu-type precipitates, whereas its effect on clusters, GP zones and θ'-phase is less pronounced.

Two types of hybrid AlMgSiCu precipitates have been found in the alloy: discrete in a bulk matrix and string-type at dislocations. Both types are strengthening, and consuming portions of alloying elements from the solid solution. However, the string type has higher nucleation/coarsening rates and a lower strength contribution, with the result of a lower overall strength of the alloy in peak and overaged conditions of the "3%-def" material. Therefore, a lower strengthening effect is caused by less homogeneous distribution and coarser morphology of the string-type precipitates compared with AlMgSiCu precipitates in the bulk matrix. Higher strengthening contribution from hybrid AlMgSiCu precipitates in the bulk superimposed on the strengthening contribution from the θ'-phase plates in the "undef" samples, provide a sharper and higher strength peak in comparison with "3%-def" sample.

Conclusions

Microstructure, hardness evolution and precipitate crystal structures in an Al-4.9Cu-0.74Mg-0.51Si-0.48Mn-0.1Cr-0.08Ti-0.02Fe alloy (in wt. %) have been investigated as a function of ageing time at 170°C. A small pre-deformation by 3%-stretching was used to introduce dislocations and understand their effect on precipitation behavior and hardness in comparison with the un-deformed alloy. The key results are summarized as follows:

(a) A small pre-deformation leads to a slight decrease in maximum strength by ~10 $HV_{0.5}$ or 15 MPa of YS in comparison with the peak-aged undeformed alloy. The negative effect of pre-deformation was associated with enhanced density of dislocations, which initiate heterogeneous nucleation and accelerated kinetics of phase transformation and growth of the AlMgSiCu-type precipitates. This process consumes a portion of alloying elements from solid solution, hindering the formation of a finer homogeneous distribution of hardening precipitates in the bulk that would have coarsened less rapidly.

(b) Pre-deformation changes the co-precipitation sequence in the studied Al-Cu-Mg-Si alloy, which can be written in dislocation-free regions as follows:

SSSS → clusters → GP+GPB + θ” + β” + β’-Cu + C → GP+GPB + θ’ + β”(+Cu) + β’-Cu + C + Q’ (*) → GPB + θ’ + C + Q’

and on dislocations as follows:

SSSS → GP + θ” + C → GP+GPB + θ” + β’-Cu + C + C1 + Q’ + S1 → GP+GPB + θ’ + β’-Cu + C + C1+ Q’ + S1 (*) → GPB + θ’ + β’-Cu + C+ C1+ Q’ + S1.

Asterisks mark the phase composition in the peak-aging state.

Strong interaction between different phases leads to the formation of hybrid structures, which can involve different number of fragments of the GP zones, θ”- and θ’-phases from the Al-Cu system, GPB zones and S1-phase from the Al-Cu-Mg system, and β”-, β’-Cu, C- and Q’-phases from the Al-Mg-Si-Cu system.

(c) A new C1-phase, isostructural to the C-phase, but differently oriented, have been found predominantly on dislocation lines. DFT calculations performed on examples of never-before-reported hybrid precipitates show that co-precipitation of these phase fragments consisting of the GP zones/GP-like structures/Cu segregations and the C-phase is energetically favorable.

These observations highlight newly discovered interaction mechanisms between the precipitates belonging to the Al-Cu(-Mg) and Al-Mg-Si(-Cu) systems and provide a better

understanding of the precipitation kinetics in industrial alloys at the border between the systems, and the expected strength potential arising from the microstructural features.

Acknowledgements

This work is financially supported by the Faculty of Natural Sciences at the Norwegian University of Science and Technology [NTNU] (Project No. 81617879) and the Ministry of Education and Science of the Russian Federation under the Agreement No. 14.584.21.0023 (ID number RFMEFI58417X0023).The TEM work was carried out on the NORTEM infrastructure (Grant 197405) at NTNU, Trondheim, Norway. The authors are grateful to the staff of the TEM Gemini Center at NTNU and the Joint Research Center at Belgorod State University for their assistance with the structural and mechanical characterizations.

References

[1] I.J. Polmear, Light alloys: from traditional alloys to nanocrystals, third ed., Butterworth-Heinemann/Elsevier, Oxford (UK), 2006.

[2] D.G. Eskin, Decomposition of supersaturated solid solutions in Al-Cu-Mg-Si alloys, J. Mater. Sci. 38 (2003) 279–290. doi:http://dx.doi.org/10.1023/A:1021109514892.

[3] D.A. Porter, K.E. Easterling, M.Y. Sherif, Phase transformations in metals and alloys, third ed., CRC press, New York, 2014.

[4] J.F. Nie, Physical Metallurgy of Light Alloys, in: Phys. Metall. Fifth Ed., fifth ed., Elsevier, 2014: pp. 2009–2156. doi:10.1016/B978-0-444-53770-6.00020-4.

[5] Q. Xiao, H. Liu, D. Yi, D. Yin, Y. Chen, Y. Zhang, B. Wang, Effect of Cu content on precipitation and age-hardening behavior in Al-Mg-Si-xCu alloys, J. Alloys Compd. 695 (2017) 1005–1013. doi:10.1016/J.JALLCOM.2016.10.221.

[6] L. Liu, J.H. Chen, S.B. Wang, C.H. Liu, S.S. Yang, C.L. Wu, The effect of Si on precipitation in Al-Cu-Mg alloy with a high Cu/Mg ratio, Mater. Sci. Eng. A. 606 (2014) 187–195. doi:10.1016/J.MSEA.2014.03.079.

[7] C. Cayron, P.A. Buffat, Transmission electron microscopy study of the β′ phase (Al–Mg–Si alloys) and QC phase (Al–Cu–Mg–Si alloys): ordering mechanism and crystallographic structure, Acta Mater. 48 (2000) 2639–2653. doi:10.1016/S1359-6454(00)00057-4.

[8] K.S. Ghosh, Calorimetric studies of 2024 Al-Cu-Mg and 2014 Al-Cu-Mg-Si alloys of various tempers, J. Therm. Anal. Calorim. 136 (2019) 447–459. doi:10.1007/s10973-018-7702-0.

[9] M. Takeda, H. Oka, I. Onaka, A new approach to the study of the GP (I) zone stability in Al-Cu alloy by means of extended Hückel molecular orbital calculations, Phys. Status Solidi. 132 (1992) 305–322. doi:10.1002/pssa.2211320207.

[10] M. Takeda, Y. Maeda, A. Yoshida, K. Yabuta, S. Konuma, T. Endo, Discontinuity of G.P.(I) zone and θ′-phase in an Al-Cu alloy, Scr. Mater. 41 (1999) 643–649. doi:10.1016/S1359-6462(99)00137-2.

[11] D. Vaughan, J.M. Silcock, Precipitates formed the orientation and shape of in an Al-Cu Alloy, 725 (1967).

[12] A. Biswas, D.J. Siegel, C. Wolverton, D.N. Seidman, Precipitates in Al-Cu alloys

revisited: Atom-probe tomographic experiments and first-principles calculations of compositional evolution and interfacial segregation, Acta Mater. 59 (2011) 6187–6204. doi:10.1016/j.actamat.2011.06.036.

[13] Z. Shen, Q. Ding, C. Liu, J. Wang, H. Tian, J. Li, Z. Zhang, Atomic-scale mechanism of the θ″ → θ′ phase transformation in Al-Cu alloys, J. Mater. Sci. Technol. 33 (2017) 1159–1164. doi:10.1016/J.JMST.2016.08.031.

[14] L. Bourgeois, C. Dwyer, M. Weyland, J.-F. Nie, B.C. Muddle, Structure and energetics of the coherent interface between the θ′ precipitate phase and aluminium in Al-Cu, Acta Mater. 59 (2011) 7043–7050. doi:10.1016/j.actamat.2011.07.059.

[15] M.R. Gazizov, A. V. Dubina, D.A. Zhemchuzhnikova, R.O. Kaibyshev, Effect of equal-channel angular pressing and aging on the microstructure and mechanical properties of an Al-Cu-Mg-Si alloy, Phys. Met. Metallogr. 116 (2015) 718–729. doi:10.1134/s0031918x15070066.

[16] I.S. Zuiko, M.R. Gazizov, R.O. Kaibyshev, Effect of thermomechanical treatment on the microstructure, phase composition, and mechanical properties of Al–Cu–Mn–Mg–Zr alloy, Phys. Met. Metallogr. 117 (2016) 906–919. doi:10.1134/s0031918x16090088.

[17] J.F. Nie, B.C. Muddle, Strengthening of an Al-Cu-Sn alloy by deformation-resistant precipitate plates, Acta Mater. 56 (2008) 3490–3501. doi:10.1016/j.actamat.2008.03.028.

[18] S.J. Andersen, C.D. Marioara, R. Vissers, A. Frøseth, H.W. Zandbergen, The structural relation between precipitates in Al-Mg-Si alloys, the Al-matrix and diamond silicon, with emphasis on the trigonal phase U1-MgAl2Si2, Mater. Sci. Eng. A. 444 (2007) 157–169. doi:10.1016/j.msea.2006.08.084.

[19] L. Arnberg, B. Aurivillius, E. Wahlström, G. Malmros, J. Sjöblom, T.G. Strand, V.F. Sukhoverkhov, The Crystal Structure of $Al_xCu_2Mg_{12-x}Si_7$, (h-AlCuMgSi)., Acta Chem. Scand. 34a (1980) 1–5. doi:10.3891/acta.chem.scand.34a-0001.

[20] C. Cayron, L. Sagalowicz, O. Beffort, P.A. Buffat, Structural phase transition in Al-Cu-Mg-Si alloys by transmission electron microscopy study on an Al-4 wt% Cu-1 wt% Mg-Ag alloy reinforced by SiC particles, Philos. Mag. A Phys. Condens. Matter, Struct. Defects Mech. Prop. 79 (1999) 2833–2851. doi:10.1080/01418619908212027.

[21] C.D. Marioara, S.J. Andersen, T.N. Stene, H. Hasting, J. Walmsley, A.T.J. Van Helvoort, R. Holmestad, The effect of Cu on precipitation in Al-Mg-Si alloys, Philos. Mag. 87 (2007) 3385–3413. doi:10.1080/14786430701287377.

[22] L. Ding, Z. Jia, J.F. Nie, Y. Weng, L. Cao, H. Chen, X. Wu, Q. Liu, The structural and compositional evolution of precipitates in Al-Mg-Si-Cu alloy, Acta Mater. 145 (2018) 437–450. doi:10.1016/j.actamat.2017.12.036.

[23] T. Saito, C.D. Marioara, S.J. Andersen, W. Lefebvre, R. Holmestad, Aberration-corrected HAADF-STEM investigations of precipitate structures in Al-Mg-Si alloys with low Cu additions, Philos. Mag. 94 (2014) 520–531. doi:10.1080/14786435.2013.857051.

[24] J.K. Sunde, C.D. Marioara, A.T.J. van Helvoort, R. Holmestad, The evolution of precipitate crystal structures in an Al-Mg-Si(-Cu) alloy studied by a combined HAADF-STEM and SPED approach, Mater. Charact. 142 (2018) 458–469. doi:10.1016/j.matchar.2018.05.031.

[25] S.J. Andersen, C.D. Marioara, J. Friis, R. Bjørge, Q. Du, I.G. Ringdalen, S. Wenner, E.A. Mørtsell, R. Holmestad, T. Saito, J. Røyset, O. Reiso, Directionality and column arrangement principles of precipitates in Al-Mg-Si-(Cu) and Al-Mg-Cu linked to line defect in Al, Mater. Sci. Forum. 877 (2016) 461–470. doi:10.4028/www.scientific.net/MSF.877.461.

[26] F.J.H. Ehlers, S. Wenner, S.J. Andersen, C.D. Marioara, W. Lefebvre, C.B. Boothroyd, R. Holmestad, Phase stabilization principle and precipitate-host lattice influences for Al-Mg-Si-Cu alloy precipitates, J. Mater. Sci. 49 (2014) 6413–6426. doi:10.1007/s10853-014-8371-4.

[27] M. Torsæter, F.J.H. Ehlers, C.D. Marioara, S.J. Andersen, R. Holmestad, Applying precipitate-host lattice coherency for compositional determination of precipitates in Al-Mg-Si-Cu alloys, Philos. Mag. 92 (2012) 3833–3856. doi:10.1080/14786435.2012.693214.

[28] M. Fiawoo, X. Gao, L. Bourgeois, N. Parson, X.Q. Zhang, M. Couper, J.F. Nie, Formation of multiple orientation relationships of Q precipitates in Al-Mg-Si-Cu alloys, Scr. Mater. 88 (2014) 53–56. doi:10.1016/j.scriptamat.2014.05.013.

[29] S.J. Andersen, H.W. Zandbergen, J. Jansen, C. Træholt, U. Tundal, O. Reiso, The

crystal structure of the β″ phase in Al-Mg-Si alloys, Acta Mater. 46 (1998) 3283–3298. doi:10.1016/S1359-6454(97)00493-X.

[30] S. Wenner, L. Jones, C.D. Marioara, R. Holmestad, Atomic-resolution chemical mapping of ordered precipitates in Al alloys using energy-dispersive X-ray spectroscopy, Micron. 96 (2017) 103–111. doi:10.1016/J.MICRON.2017.02.007.

[31] J.K. Sunde, C.D. Marioara, A.T.J. van Helvoort, R. Holmestad, The evolution of precipitate crystal structures in an Al-Mg-Si(-Cu) alloy studied by a combined HAADF-STEM and SPED approach, Mater. Charact. 142 (2018) 458–469. doi:10.1016/j.matchar.2018.05.031.

[32] S. Wenner, C.D. Marioara, S.J. Andersen, M. Ervik, R. Holmestad, A hybrid aluminium alloy and its zoo of interacting nano-precipitates, Mater. Charact. 106 (2015) 226–231. doi:10.1016/j.matchar.2015.06.002.

[33] T. Saito, F.J.H. Ehlers, W. Lefebvre, D. Hernandez-Maldonado, R. Bjørge, C.D. Marioara, S.J. Andersen, E.A. Mørtsell, R. Holmestad, Cu atoms suppress misfit dislocations at the β″/Al interface in Al-Mg-Si alloys, Scr. Mater. 110 (2016) 6–9. doi:10.1016/j.scriptmat.2015.07.033.

[34] C.R. Hutchinson, S.P. Ringer, Precipitation processes in Al-Cu-Mg alloys microalloyed with Si, Metall. Mater. Trans. A. 31 (2000) 2721–2733. doi:10.1007/BF02830331.

[35] S.C. Wang, M.J. Starink, Precipitates and intermetallic phases in precipitation hardening Al–Cu–Mg–(Li) based alloys, Int. Mater. Rev. 50 (2005) 193–215. doi:10.1179/174328005X14357.

[36] L. Kovarik, S.A. Court, H.L. Fraser, M.J. Mills, GPB zones and composite GPB/GPBII zones in Al-Cu-Mg alloys, Acta Mater. 56 (2008) 4804–4815. doi:10.1016/j.actamat.2008.05.042.

[37] Y.A. Bagaryatsky, Mechanism of artificial aging of alloy Al-Cu-Mg, Dokl. Akad. SSSR. 87 (1952) 397–401.

[38] Y.A. Bagaryatsky, On the nature of natural aging of aluminium alloys, Dokl. Akad. Nauk SSSR. 87 (1952) 559–562.

[39] L. Kovarik, M.J. Mills, Ab initio analysis of Guinier-Preston-Bagaryatsky zone nucleation in Al-Cu-Mg alloys, Acta Mater. 60 (2012) 3861–3872.

doi:10.1016/j.actamat.2012.03.044.

[40] M.J. Styles, C.R. Hutchinson, Y. Chen, A. Deschamps, T.J. Bastow, The coexistence of two S (Al_2CuMg) phases in Al-Cu-Mg alloys, Acta Mater. 60 (2012) 6940–6951. doi:10.1016/j.actamat.2012.08.044.

[41] Z. Feng, Y. Yang, B. Huang, X. Luo, M. Li, Y. Chen, M. Han, M. Fu, J. Ru, HRTEM and HAADF-STEM tomography investigation of the heterogeneously formed S (Al_2CuMg) precipitates in Al–Cu–Mg alloy, Philos. Mag. 93 (2013) 1843–1858. doi:10.1080/14786435.2012.762469.

[42] T. Saito, E.A. Mørtsell, S. Wenner, C.D. Marioara, S.J. Andersen, J. Friis, K. Matsuda, R. Holmestad, Atomic structures of precipitates in Al-Mg-Si alloys with small additions of other elements, Adv. Eng. Mater. 20 (2018) 1800125. doi:10.1002/adem.201800125.

[43] D.B. Williams, B.C. Carter, Transmission electron microscopy, second ed., Springer, New York, 2009.

[44] M. Gazizov, R. Kaibyshev, Precipitation structure and strengthening mechanisms in an Al-Cu-Mg-Ag alloy, Mater. Sci. Eng. A. 702 (2017) 29–40. doi:10.1016/j.msea.2017.06.110.

[45] P.D. Nellist, S.J. Pennycook, The principles and interpretation of annular dark-field Z-contrast imaging, in: 2000: pp. 147–203. doi:10.1016/S1076-5670(00)80013-0.

[46] G. Kresse, J. Hafner, Ab initio molecular dynamics for open-shell transition metals, Phys. Rev. B. 48 (1993) 13115–13118. doi:10.1103/PhysRevB.48.13115.

[47] G. Kresse, D. Joubert, From ultrasoft pseudopotentials to the projector augmented-wave method, Phys. Rev. B. 59 (1999) 11–19. doi:10.1103/PhysRevB.59.1758.

[48] M. Methfessel, A.T. Paxton, High-precision sampling for Brillouin-zone integration in metals, Phys. Rev. B. 40 (1989) 3616–3621. doi:10.1103/PhysRevB.40.3616.

[49] S.C. Wang, M.J. Starink, Precipitates and intermetallic phases in precipitation hardening Al-Cu-Mg-(Li) based alloys, Int. Mater. Rev. 50 (2005) 193–215. doi:10.1179/174328005X14357.

[50] H. Zhang, D.H. Wang, K.H. Kuo, Icosahedral and decagonal quasicrystals, crystalline phases, and multiple twins in rapidly solidified $Al_{13}Cr_4Si_4$, J. Mater. Sci. 24 (1989) 2981–2986. doi:10.1007/BF02385657.

[51] L. Kovarik, P.I. Gouma, C. Kisielowski, S. a. Court, M.J. Mills, A HRTEM study of metastable phase formation in Al–Mg–Cu alloys during artificial aging, Acta Mater. 52 (2004) 2509–2520. doi:10.1016/j.actamat.2004.01.041.

[52] K. Teichmann, C.D. Marioara, S.J. Andersen, K.O. Pedersen, S. Gulbrandsen-Dahl, M. Kolar, R. Holmestad, K. Marthinsen, HRTEM study of the effect of deformation on the early precipitation behaviour in an AA6060 Al-Mg-Si alloy, Philos. Mag. 91 (2011) 3744–3754. doi:10.1080/14786435.2011.593577.

[53] S. Wenner, J. Friis, C.D. Marioara, S.J. Andersen, R. Holmestad, Structural modifications and electron beam damage in aluminium alloy precipitate θ'-AL2, Philos. Mag. 95 (2015) 3524–3534. doi:10.1080/14786435.2015.1090639.

[54] S. Samson, Ø. Ellefsen, O. Hassel, A. Kainulainen, A. Halonen, E. Pulkkinen, Die Kristallstruktur von $Mg_2Cu_6Al_5$, Acta Chem. Scand. 3 (1949) 809–834. doi:10.3891/acta.chem.scand.03-0809.

Table 1. Overview of known phases in Al-Cu, Al-Cu-Mg and Al-Mg-Si-Cu systems

Phase	Nominal composition	Morphology	Crystal structure	Orientation relationships (OR)
Al-Cu alloys				
GP zones (GPI)	Cu	Plate	Monoatomic layers parallel to $\{001\}_{Al}$ planes [9,34]	-
θ'' (GPII)	Al_3Cu-Al_2Cu	Plate	Tetragonal, $a = b = 0.404$ nm, $c = 0.790$ nm - three Al layers sandwiched by two single Cu layers and parallel to $\{001\}_{Al}$ planes [3,4,12,34]	-
θ'	Al_2Cu	Plate	I-4m2, $a = b = 0.405$ nm, $c = 0.580$ nm	$(001)_{θ'}//(001)_{Al}$, $[100]_{θ'}//[100]_{Al}$ [11–14,34]
θ	Al_2Cu	-	I4/mcm, $a = b = 0.607$ nm, $c = 0.4877$ nm	22 independent ORs [34]
Al-Cu-Mg alloys				
GPB zone	-	Rods	Rod-like structural units along $<001>_{Al}$ [34–38]	-
S''	-	Rods	Distorted S-phase	$[100]_{Al}//[100]_{S''}$, $[0\text{-}53]_{Al}//[011]_{S''}$, $[011]_{Al}//[013]_{S''}$ [34–37]
S'	-	Laths	Distorted S-phase [34,39]	-
S1	Al_2CuMg	Laths	Cmcm, $a = 0.405$ nm, $b = 0.925$, $c = 0.709$ nm [39]	$(001)_{S1}//(021)_{Al}$, $[100]_{S1}//[100]_{Al}$ [39]
S2	Al_2CuMg	Rods	Cmcm, $a = 0.402$ nm, $b = 0.927$, $c = 0.712$ nm [39]	S2-type: $(041)_{S2}//(02\text{-}1)_{Al}$, $[100]_{S2}//[100]_{Al}$ [39,40]
S	Al_2CuMg	Different [39]	Cmcm, $a = 0.400$ nm, $b = 0.923$, $c = 0.714$ nm [34]	12 ORs referred in work [34]
σ	$Al_5Cu_6Mg_2$	Cubes	Pm3, $a = 1.999$ nm [42,43]	$\{001\}_{σI}//\{001\}_{Al}$, $<100>_{σI}//<100>_{Al}$ [43,44] and $\{010\}_{σII}//\{100\}_{Al}$, $<001>_{σII}//<001>_{Al}$ [44]
Al-Mg-Si-Cu alloys				
GP zones (pre-β'')	from $Mg_2Al_3Si_2$ to $Mg_{2+x}Al_{7-x-y}Si_{2+y}$ ($1<x$, $y<3$)	Rods	Structure close to β'' [21]	-
β''	$Mg_{6-x}Al_{1+x}Si_4$ (x=0,1,2)	Rods	C2/m, $a = 1.516$ nm, $b = 0.405$ nm, $c = 0.674$ nm, $\beta = 105.3°$	$(010)_{β''}//\{100\}_{Al}$, $[001]_{β''}//<013>_{Al}$, $[100]_{β''}//<032>_{Al}$ [30,41]
β'-Cu	$Al_3Mg_3Si_2Cu$	Rods	Hexagonal P-62m, $a = b = 0.690$ nm, $c = 0.405$ nm	$(001)_{β'\text{-}Cu}//(001)_{Al}$, $[100]_{β'\text{-}Cu}//[310]_{Al}$, $[010]_{β'\text{-}Cu}//[1\text{-}50]_{Al}$ [21,41]
QP	Unknown	Rods	Latent disordered structure constituted from Cu triangular clusters [7]	OR1: $[001]_{QP}//[001]_{Al}$, $(100)_{QP}//(110)_{Al}$, OR2: $[001]_{QP}//[001]_{Al}$, $(100)_{QP}//(100)_{Al}$ [7]
QC	Unknown	Rods	Ordered hexagonal $P\bar{6}2m$, $a = 0.670$ nm, $c = 0.405$ nm (similar to the β'-Cu phase) [7,20]	$[001]_{QC}//[001]_{Al}$, $(100)_{QC}//(110)_{Al}$ [20]
C	$Mg_4AlSi_{3.3}Cu_{0.7}$	Plates	Monoclinic P21/m, $a = 1.032$ nm, $b = 0.405$ nm, $c = 0.810$ nm, $\beta_C = 100.9°$	$[001]_{C}//[001]_{Al}$, $(010)_{C}//(010)_{Al}$ [21,27]
L	Variable	Laths	Disordered version of the C-phase [21]	-
Si	Unknown	Rods	Hexagonal $P\bar{6}2m$ (disordered with Si-network) [21]	-
Q'	Probably $Al_3Cu_2Mg_9Si_7$	Rods/laths	Hexagonal $P\bar{6}$, $a = b = 1.032$ nm, $c = 0.405$ nm, $\gamma = 120°$	$(21\text{-}30)_{Q'}//(100)_{Al}$, $[0001]_{Q'}//[001]_{Al}$ or $(11\text{-}20)_{Q'}//(010)_{Al}$, $[0001]_{Q'}//[001]_{Al}$ [21]
Q	$Al_xCu_2Mg_{12-x}Si_7$, $3\leq x\leq 5$	Rods	Hexagonal $P\bar{6}$, $a = b = 1.039$ nm, $c = 0.405$ nm, $\gamma = 120°$ [19]	6 ORs referred in work [29]

Table 2. Phase evolution in studied alloy

Aging state	Phases belonging to alloy systems		
	Al-Cu	Al-Cu-Mg	Al-Mg-Si-Cu
In dislocation-free regions			
Under-aging (0.25 h)	Clusters	-	-
Under-aging (1 h)	GP + θ”	GPB	β” + β’-Cu + C
Peak-aging (16 h)	GP + θ’		β”(+Cu) + β’-Cu + C + Q’*
Over-aging (96 h)	θ’		C + Q’
On dislocation lines			
Under-aging (0.25 h)	GP + θ”	-	C
Under-aging (1 h)		GPB + S1	β’-Cu + C + C1 + Q’
Peak-aging (16 h)	GP + θ’		
Over-aging (96 h)	θ’		

* C1-phase was excluded from the precipitation sequence in dislocation-free regions because fragments of this phase have been rarely found there.

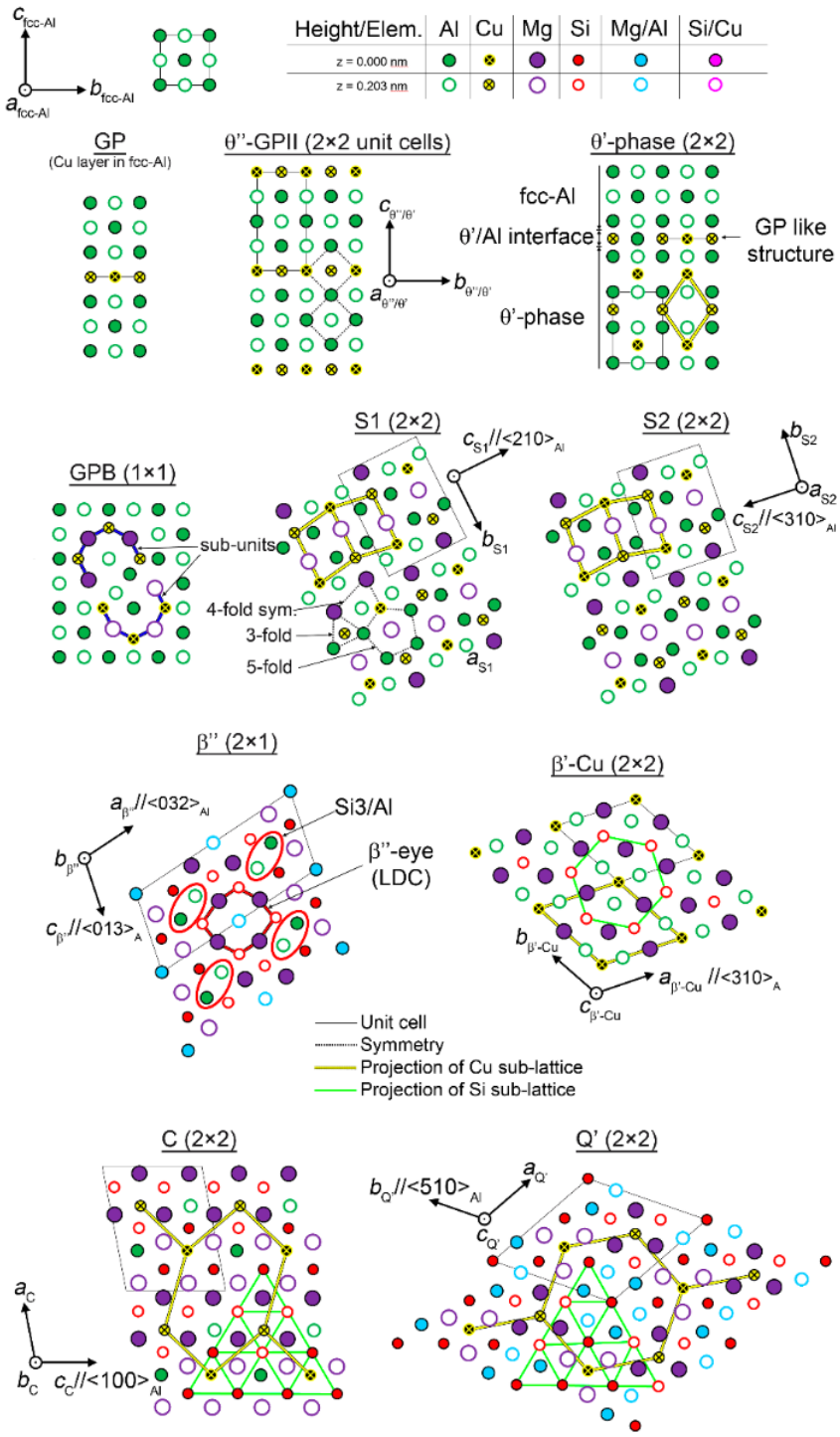

Fig. 1 Schematic of atomic positions in the unit cells of metastable ordered precipitates in Al-Cu, Al-Cu-Mg and Al-Si-Mg-Cu alloys. All phases are drawn using the same scale. Filled/open circles denote different positions along the paper plane normal, corresponding to a separation of 0.5 × the lattice parameter of Al.

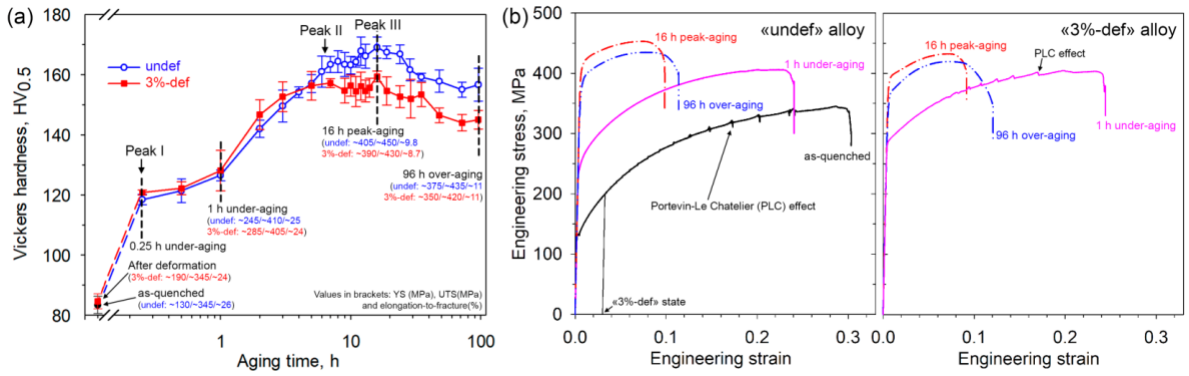

Figure 2. Age-hardening curves (a) for the alloy in “undef” and “3%-def” conditions and typical engineering stress-strain curves (b) for some specific aging conditions. Aging durations indicated by vertical dashed lines on the aging curves were chosen for TEM characterization.

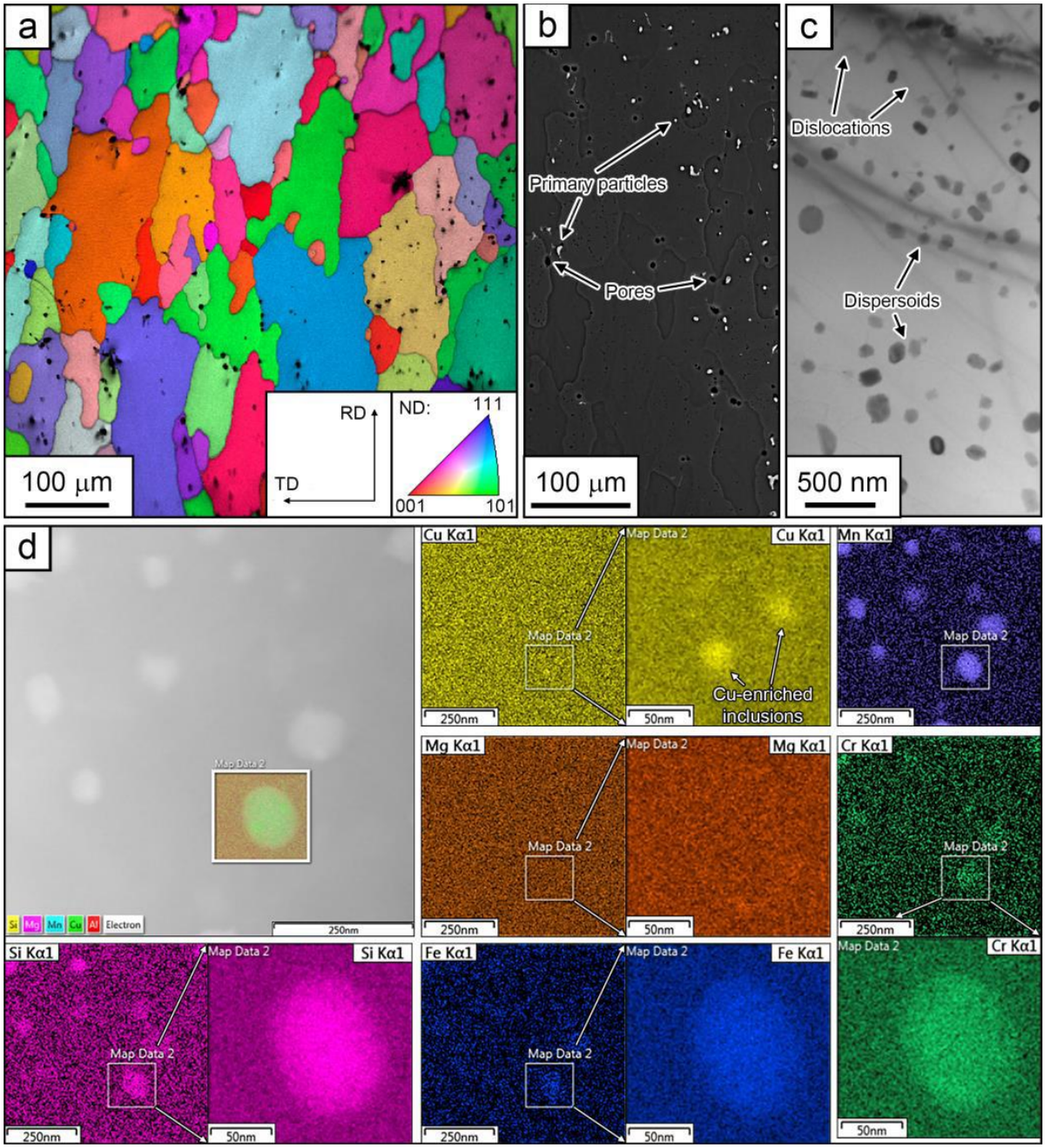

Figure 3. Microstructure of the alloy in as-quenched condition. Overlay of OIM and IQ maps (a), BSE-SEM (b) and bright-field TEM images (c). In OIM map, pixels with lower IQ values are dark showing presence of porosity and distributions of primary particles. Element maps (EDS-STEM) for a selected group of dispersoids (d).

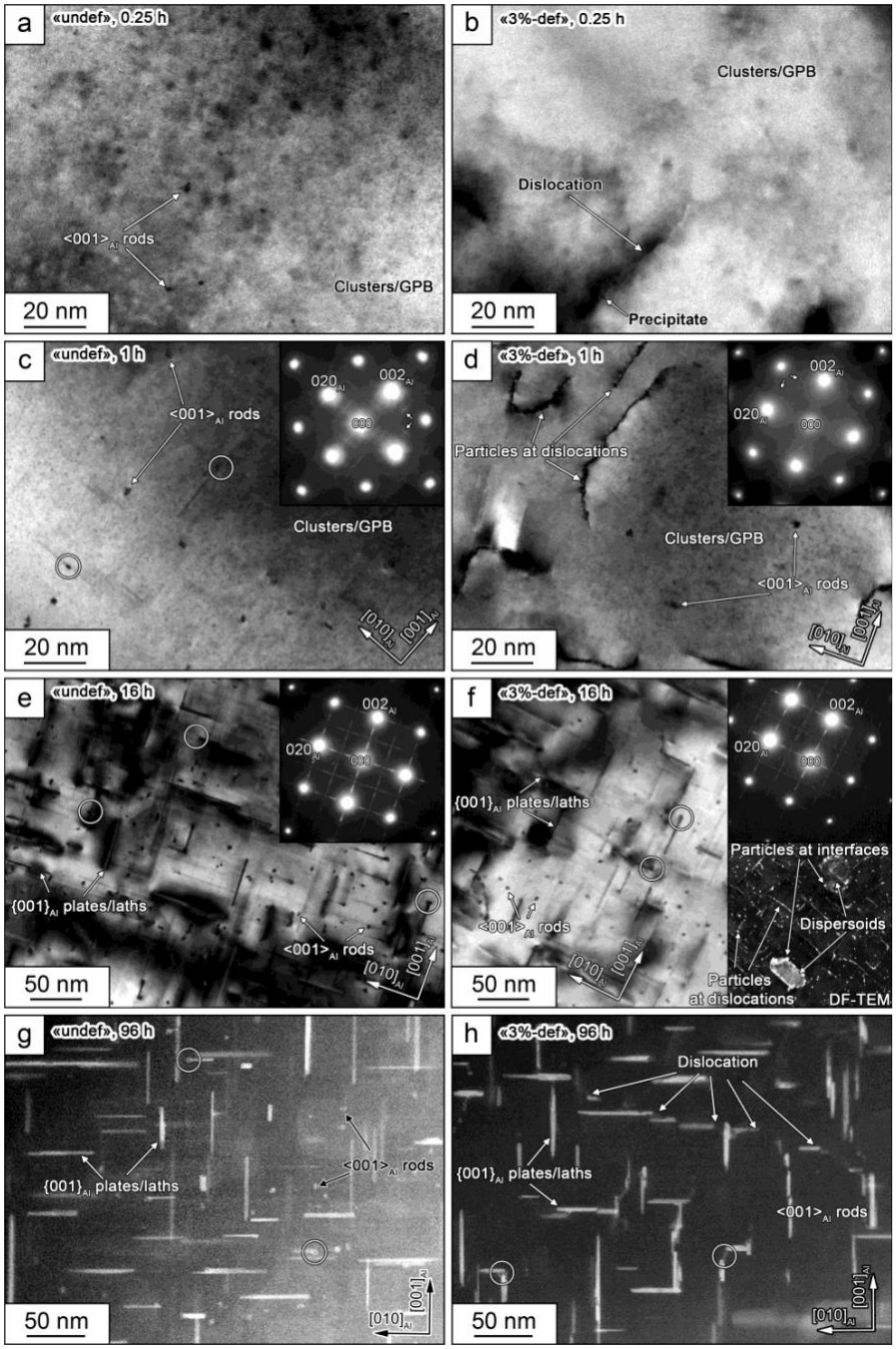

Figure 4. BF-TEM (a-f) and HAADF-STEM images (g-h) of the typical microstructure of the “undef” (a, c, e, g) and “3%-def” samples (b, d, f, h) aged at 170°C for different times: 0.25 h under-aged (a, b), 1 h under-aged (c, d), 16 h peak-aged (e, f) and 96 h over-aged (g, h). Dark/bright spots and lines in BF-TEM/HAADF-STEM images represent cross sections of the rod- and lath-/plate-like precipitates, respectively, normal to the image plane.

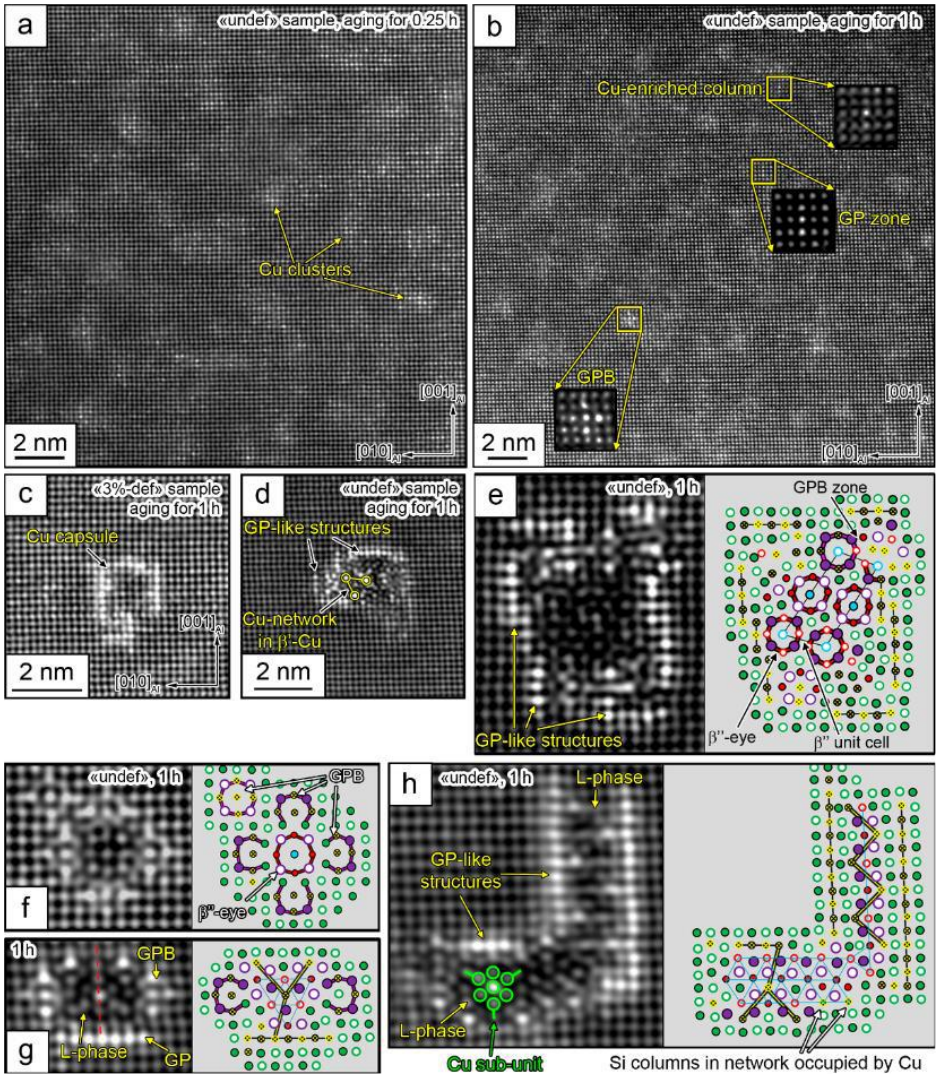

Figure 5. HAADF-STEM images of precipitates in bulk material in under-aging state. Clusters (a); GP zones, Cu-enriched columns and GPB zone units (b); Cu capsule (c); hybrid precipitates consisting of disordered L-phase and GP-like structures (d), β''-phase fragment and GP-like structures (e), β''-eye and five GPB zone units (f), L-phase, two GPB zone units and GP-like structures (g), L-phase and GP-like structures (h). The Cu- and Si-networks are marked by yellow and blue-green lines, respectively, in the suggested atomic models (see legend in Fig. 1).

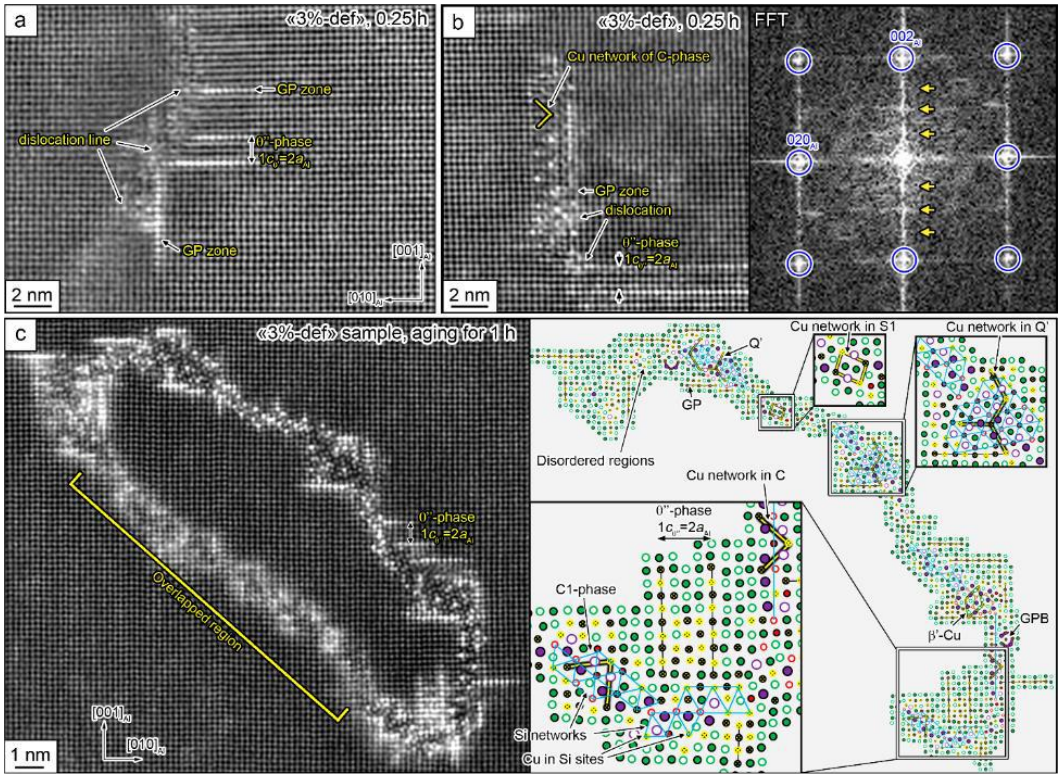

Figure 6. HAADF-STEM images of hybrid precipitates continuously decorating dislocation lines in under-aging state. The Cu- and Si-networks are marked by yellow and blue-green circles/lines, respectively, in the suggested atomic models (see legend in Fig. 1). Yellow arrows in FFT pattern show streaks distribution typical for the L-phase [37]. The *fcc*-Al spots are marked by blue circles in FFT pattern.

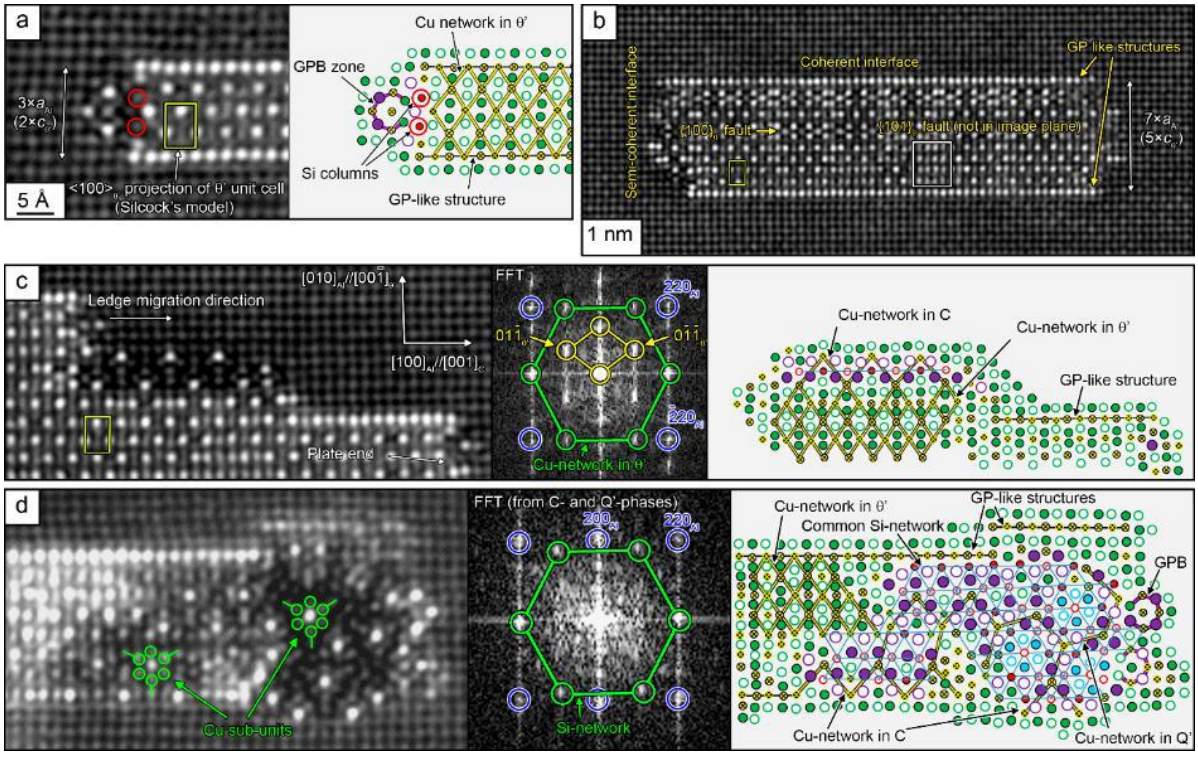

Figure 7. HAADF-STEM images of precipitates and hybrid structures in peak-aging state. Thin θ'-phase plate and GPB zone units with possible Si columns (marked by red circles) in transition region (a). Thick θ'-phase plate with $\{100\}_{\theta'}$ and $\{101\}_{\theta'}$ faults (b). Hybrid structures showing interaction between θ'-phase plates and AlMgSiCu precipitates (c, d). The Cu- and Si-networks are marked by yellow and blue-green lines, respectively, in the suggested atomic models (see legend in Fig. 1). Green hexagon in FFT patterns shows the symmetry and orientation of the Cu sub-units in the L- and C-phases.

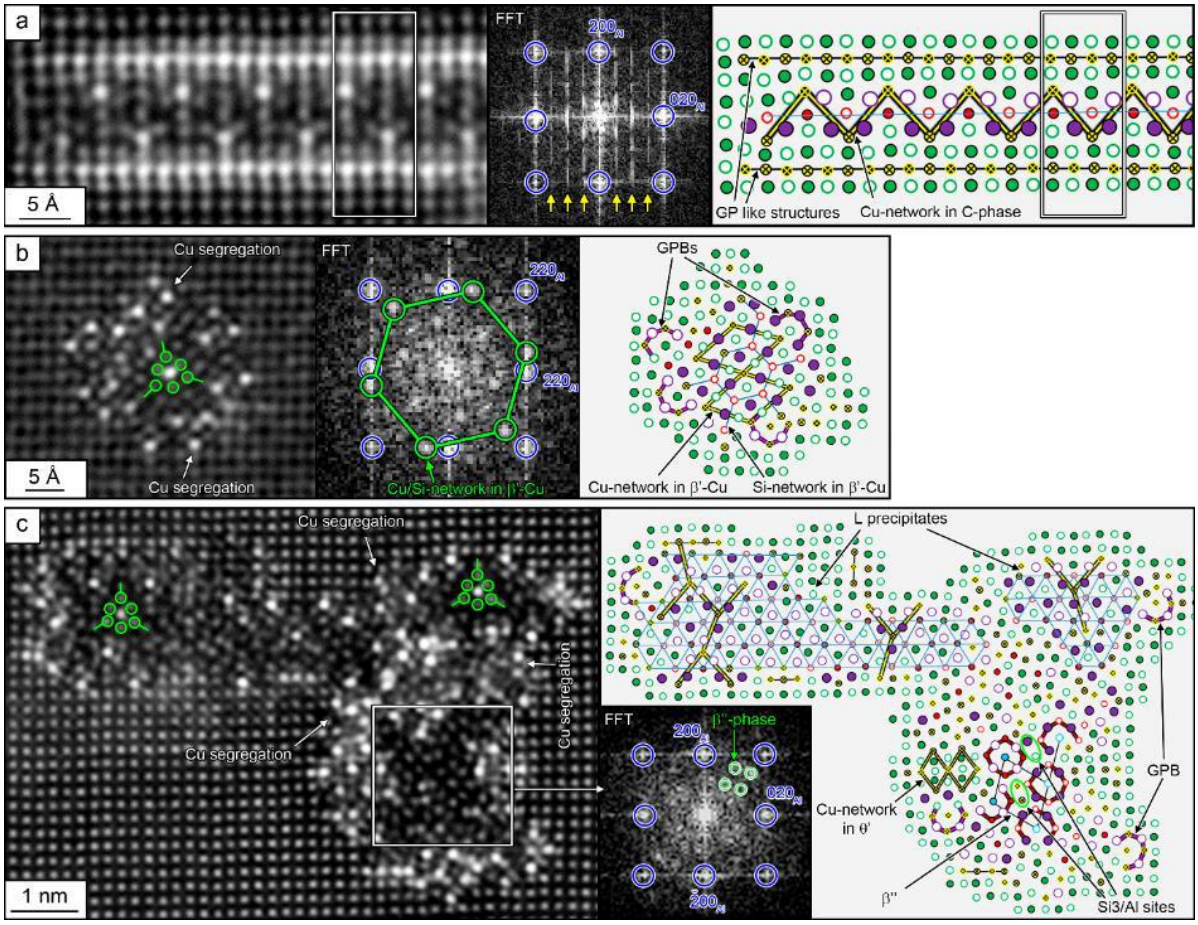

Figure 8. HAADF-STEM images of hybrid precipitates in peak-aging state. Hybrid structures showing interaction between C-phase and GP-like structures (a), β'-Cu and GPB zone units (b), C-, β''- and θ'-phase fragments (c). The Cu- and Si-networks are marked by yellow and blue-green lines, respectively, in the suggested atomic models (see legend in Fig. 1).

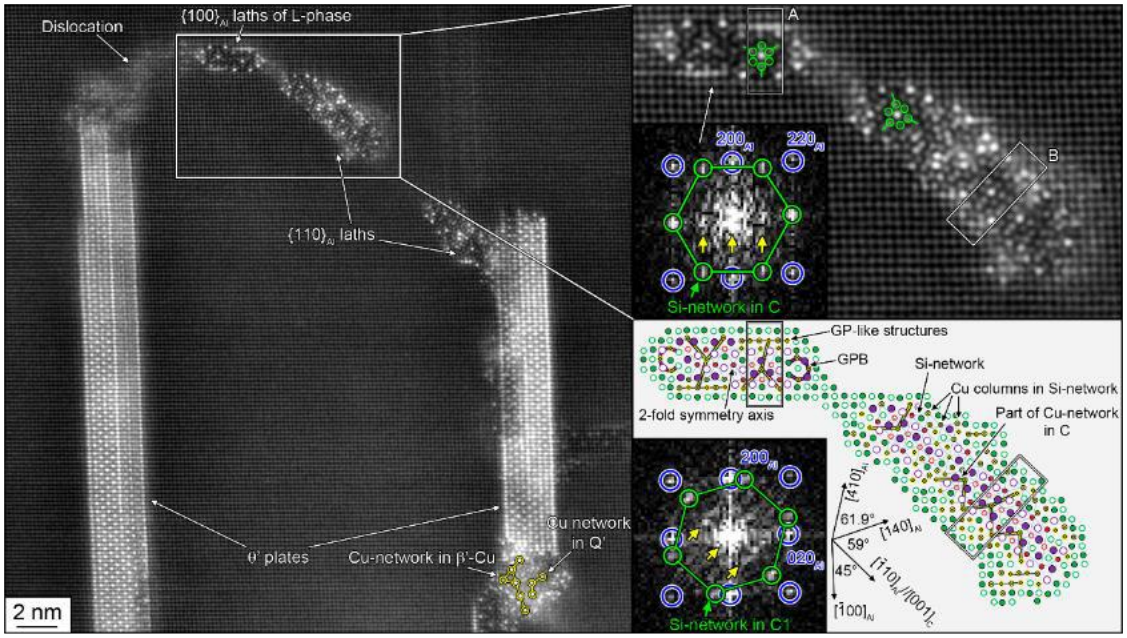

Figure 9. HAADF-STEM images of hybrid precipitates continuously decorating dislocation lines in “3%-def” alloy in peak-aging state. The Cu- and Si-networks are marked by yellow and blue-green lines, respectively, in the suggested atomic model (see legend in Fig. 1). Green hexagons in FFT patterns shows the orientation of the Si-networks in the L (or C fragments) and C1-phases. The *fcc*-Al spots are marked by blue circles.

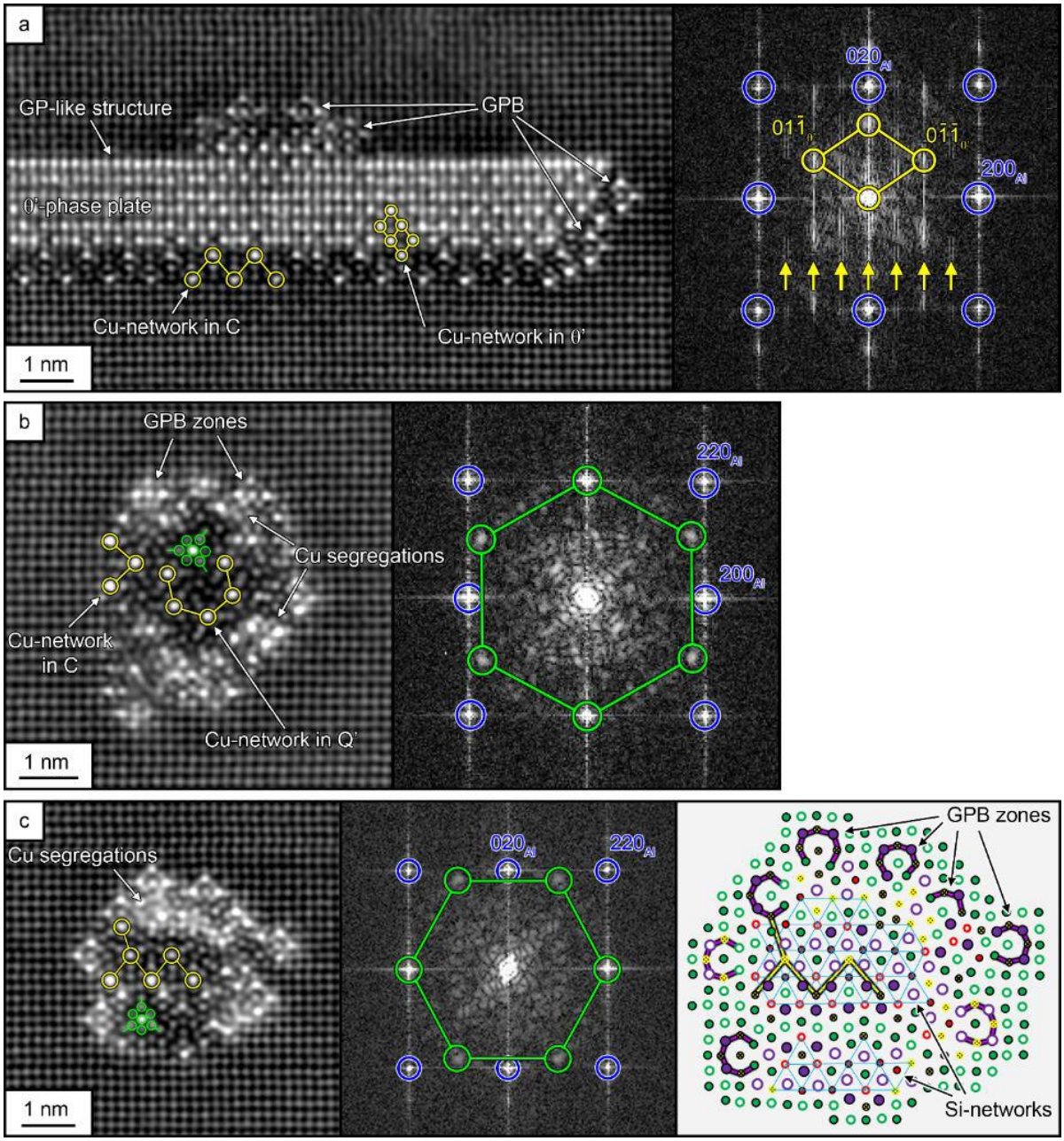

Figure 10. HAADF-STEM images of hybrid precipitates in over-aging state. Hybrid precipitates consisting of the θ'-phase, C-phase and GPB zone units (a), the Q'-, C-phase fragments and GPB zone units (b), disordered L-phase surrounded by the GPB zone units (c). The Cu- and Si-networks are marked by yellow and blue-green lines, respectively, in the suggested atomic model (see legend in Fig. 1). Green hexagons in the FFT patterns show Si-networks in the C- and Q'-phase fragments.

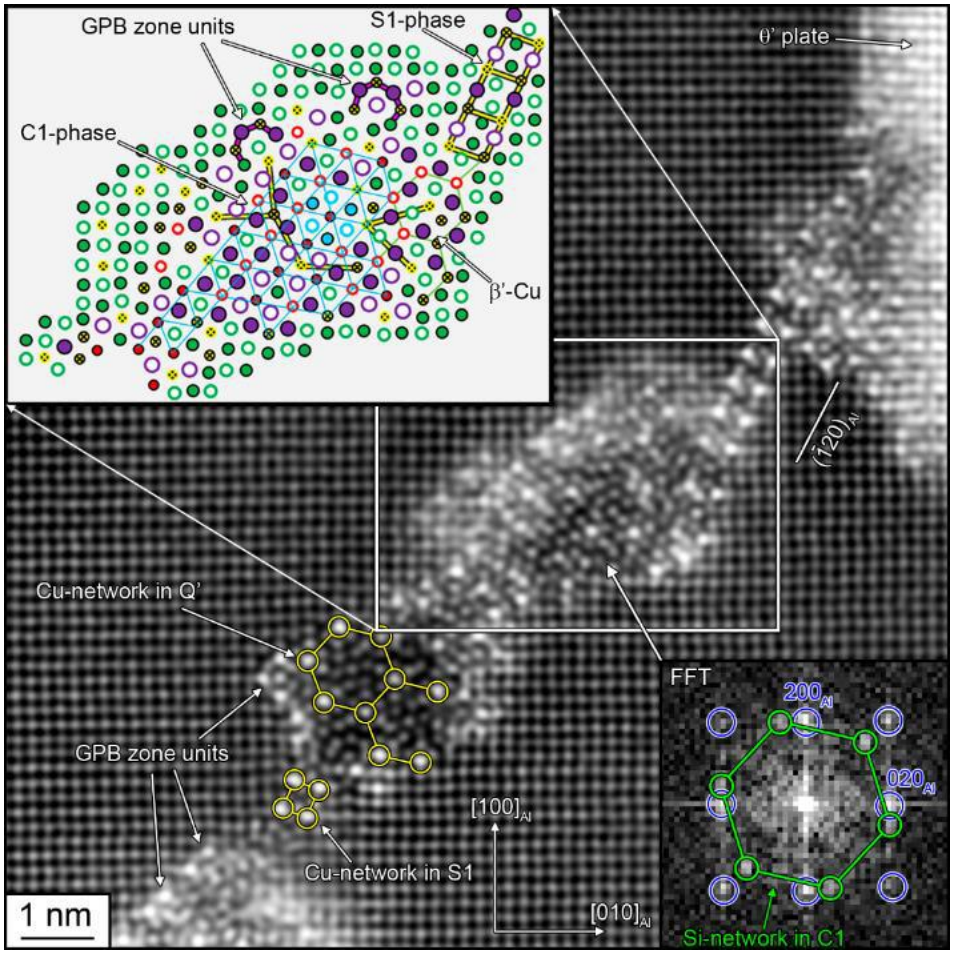

Figure 11. HAADF-STEM images of hybrid precipitates continuously decorating dislocation lines in “3%-def” alloy in over-aging state. The Cu-networks marked by yellow circles/lines are in Q’- and S1-phases. The Cu- and Si-networks are marked by yellow and blue-green lines, respectively, in the suggested atomic model (see legend in Fig. 1). Green hexagon in the FFT pattern shows Si-network in Q’-phase.

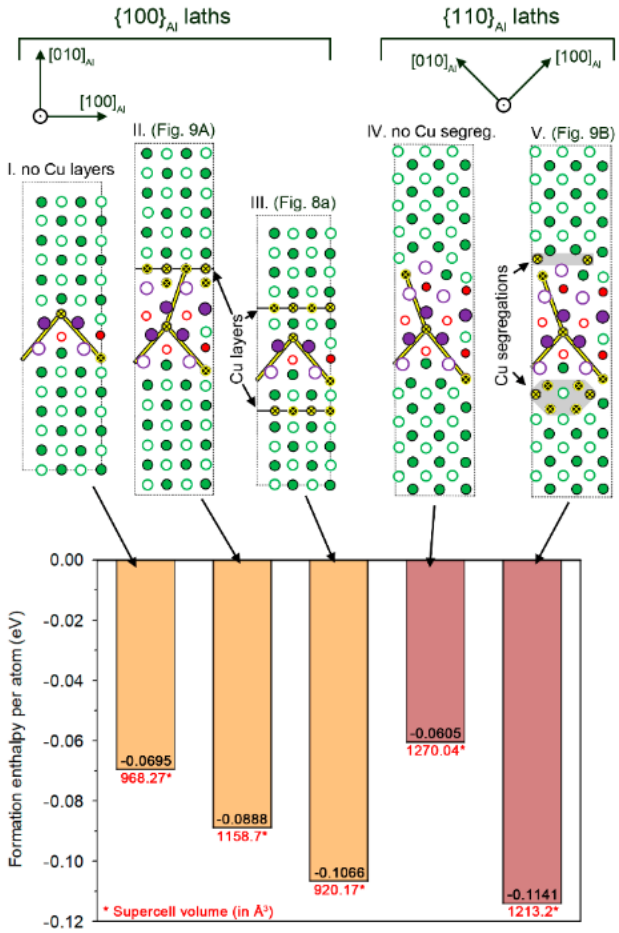

Figure 12. DFT calculations showing the formation enthalpy per atom (eV) for different lath-shaped precipitates of C-/L-phase having different orientations and Cu segregations – layers along interfacial boundaries. Structures I/II/III and IV/V are $\{200\}_{Al}$ and $\{220\}_{Al}$ laths, respectively. Structures II and III have Cu layers along one and both board interface sides, respectively. There are no experimental observations of Structure I and IV in studied alloy.

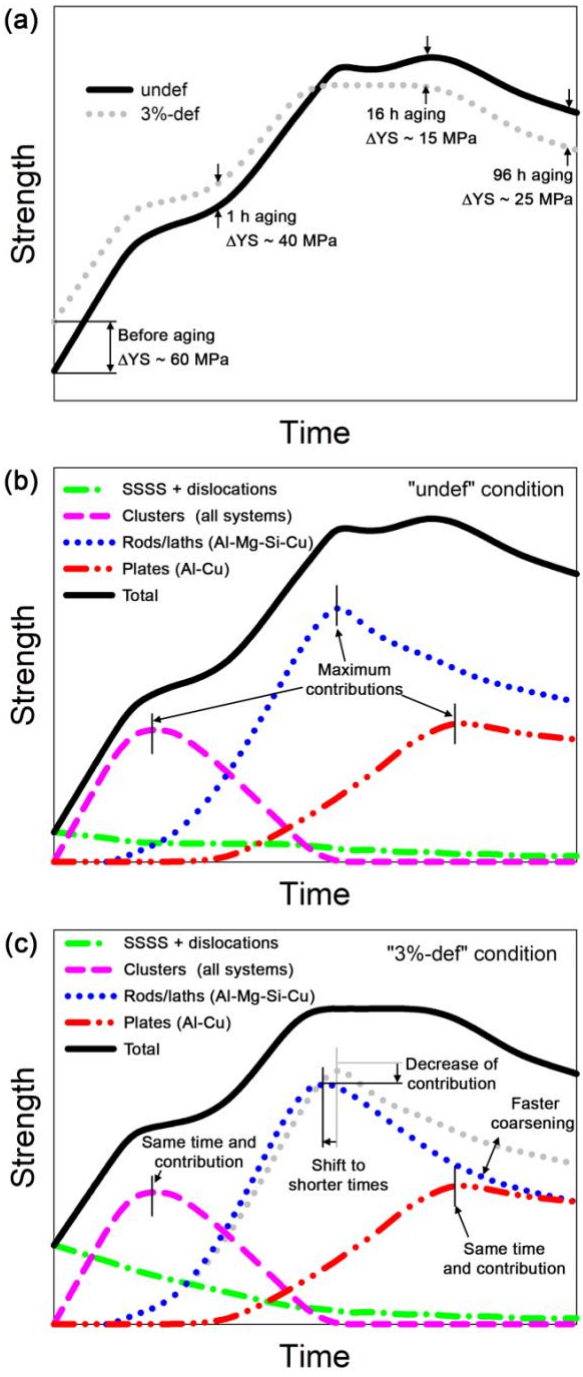

Figure 13. Schematic strength evolution in the alloy (a) and strength contributions in “undef” (b) and “3%-def” states (c) during aging. Three stages of precipitate strengthening evolutions have been classified and related with the formation of clusters (from all alloying systems), rods/laths (AlMgSiCu-type precipitates) and plates (θ’-phase from Al-Cu system). The solid solution and dislocation strengthenings were combined for simplicity.